Brain development: machine learning analysis of individual stem cells in live 3D tissue

Martin Hailstone[1#], Lu Yang[1#], Dominic Waithe[2#], Tamsin J Samuels[1], Yoav Arava[3], Tomasz Dobrzycki[1,4], Richard M Parton[1*] and Ilan Davis[1*]

Affiliations

[1] Department of Biochemistry
University of Oxford
South Parks Road
Oxford OX1 3QU, UK

[2] Wolfson Imaging Center
Weatherall Institute for Molecular Medicine
University of Oxford
Oxford, UK

[3] Department of Biology
Technion – Israel Institute of Technology
Haifa 32000

[4] Current address:
Weatherall Institute for Molecular Medicine
University of Oxford
Oxford, UK

* **Correspondence:** richard.parton@bioch.ox.ac.uk; ilan.davis@bioch.ox.ac.uk
\# Contributed equally

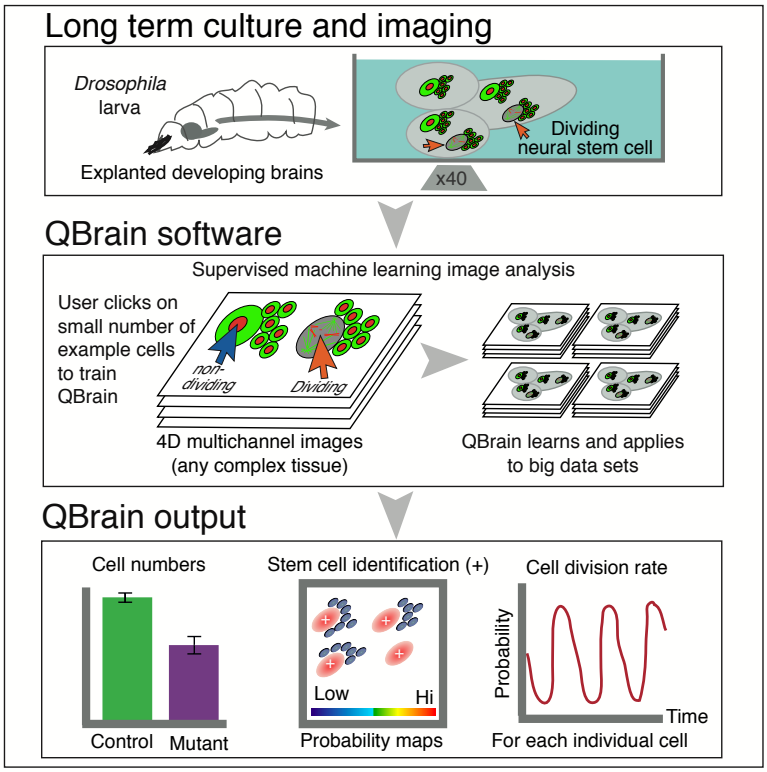

In Brief

We have optimised imaging of explanted *Drosophila* brains and developed novel 4D machine learning image analysis software that out performs existing methods in characterising brain malformation mutants. Our new techniques can be applied widely to analyse the development of complex tissues in terms of the behaviour of individual cells.

Highlights

- Time-lapse imaging of developing ex-vivo cultured brains in excess of 30 hours
- QBrain: machine learning quantitation of cell types and division in complex tissue
- Outperforms other state-of-the-art machine learning image analysis tools
- Automated characterisation of cause of a complex enlarged mutant brain phenotype

Key words: Bio-image Informatics; automated analysis; 4D; supervised machine learning; random forest; mutant phenotypes; *ex-vivo* culture; neural stem cells; Neuroblast; *Drosophila*

SUMMARY

Brain malformations often result from subtle changes in neural stem cell behaviour, which are difficult to characterise using current methods on fixed material. Here, we tackle this issue by establishing optimised approaches for extended 3D time-lapse imaging of living explanted *Drosophila* brains and developing QBrain image analysis software, a novel implementation of supervised machine learning. We combined these tools to investigate brain enlargement of a previously difficult to characterise mutant phenotype, identifying a defect in developmental timing. QBrain significantly outperforms existing freely available state-of-the-art image analysis approaches in accuracy and speed of cell identification, determining cell number, location, density and division rate from large 3D time-lapse datasets. Our use of QBrain illustrates its wide applicability to characterise development in complex tissue, such as tumours or organoids, in terms of the behaviour in 3D of individual cells in their native environment.

INTRODUCTION

The human brain develops through the regulated proliferation and differentiation of a small number of neural stem cells, leading to a vast and diverse population of neurons and glia (Kohwi & Doe, 2013). Elucidating the molecular basis of these processes is important for basic neuroscience and critical for discovering new treatments for neurological diseases. However, this goal is daunting due to the huge complexity of the human brain, which consists of 10^{11} neurons, and the difficulty of imaging mammalian brains at cellular resolutions using light microscopy. Simpler model systems offer a way forward, as whole zebrafish and *Drosophila* brains can be effectively imaged at the cellular level (Barbosa & Ninkovic, 2016; Dray *et al*., 2015; Medioni *et al*., 2015; Rabinovich *et al*., 2015; Cabernard & Doe., 2013; Graeden & Sive, 2009). Of these two models, *Drosophila* has been characterised more extensively, using genetic screens for genes that regulate brain development (Li *et al*., 2016; Neumüller *et al*., 2011; Perrimon *et al.,* 2010; Patton & Zon, 2001). The *Drosophila* larval brain contains 10^4 neurons, can be cultured *ex-vivo* and imaged using standard fluorescence

microscopy (Cabernard & Doe., 2013; Prithviraj *et al*., 2012). In the larval central brain (CB), neural stem cells, also known as neuroblasts (NBs), undergo asymmetric division to produce another stem cell and a ganglion mother cell (GMC). GMCs terminally divide to produce a pair of cells that differentiate to become neurons or glia (Homem & Knoblich, 2012). These divisions are highly regulated and defects in the process can result in under-proliferation or over-proliferation, which can lead to cancer-like phenotypes (reviewed in Homem *et al.,* 2015; Laurenson *et al*., 2013; see also Narbonne-Reveau *et al*., 2016; Laurenson *et al*., 2013; Miles *et al*., 2011; Chia *et al*., 2008; Bello *et al*., 2006; Caussunus & Gonzalez, 2005).

Functional screens in *Drosophila* have significantly extended the number of components known to regulate NB proliferation and differentiation leading to defects in brain size or tumour formation (Berger *et al*., 2012; Homem & Knoblich, 2012; Neumüller *et al*., 2011). Such screens have the power of genome wide coverage, but, to be effective, often require time-consuming detailed manual characterisation of phenotypes that are frequently subtle and complex. One such mutant phenotype, is that of the conserved RNA binding protein Syncrip (Syp), previously described as exhibiting a very weak NB under-proliferation in a high-throughput screen of genes affecting brain development (Neumüller *et al*., 2011). SYNCRIP/hnRNPQ, the mammalian homologue of Syp, has interesting roles in mammalian hippocampal cells. Syp also determines neuronal fate in the *Drosophila* brain (Ren *et al*., 2017; Liu *et al*., 2015) and is required for neuromuscular junction development and function (McDermott *et al*., 2014; Halstead *et al*., 2014). Much of the work characterising the *syp* phenotype and the developmental defects of other neuronal mutants has relied on immuno-labelling of fixed material in which cell types must be identified manually from fixed “snapshots” of the developing brain, or from disaggregated cells in culture (Ren *et al*., 2017; Homem *et al*., 2014; 2013; Moraru *et al*., 2012; Berger *et al.,* 2012; Wu & Luo, 2006; Savoian & Rieder, 2002; Furst & Mahowald, 1985). This reliance on fixed material and largely manual analysis constitutes a significant limitation to progress in the field.

MOTIVATION AND DESIGN

Here, we describe our development of an optimised live-imaging method for *Drosophila* larval brains and a generally applicable, novel machine learning image analysis tool for characterising

complex tissue development at the cellular level.

In general, live-imaging allows a more definitive characterisation of subtle mutant phenotypes (Homem *et al*., 2014; 2013; Walker, 1954) than can be achieved in fixed material. However, the ability to track and quantitate the proliferation and differentiation of individual cells in intact living brains remains a major unsolved experimental challenge. To date, culturing and imaging of living explanted *Drosophila* larval brains has only been partially successful (Cabernard & Doe, 2013; Prithviraj *et al*., 2012). Moreover, progress in the field of brain development is further limited by the lack of image analysis methods for high-throughput automated identification of cells and their pattern of divisions and differentiation (Schmitz *et al*., 2014; Myers, 2012; Neumüller *et al.,* 2011; Scott & Baier, 2009). Existing automated methods can identify cells in 3D images, but lack the flexibility, speed and ease of use to make them effective solutions for time-lapse movies as large and complex as a whole developing brain (Lou *et al*., 2014; Cabernard & Doe, 2013; Homem *et al*., 2013; Meijering, 2012; Meijering *et al*., 2012).

Our optimised culture and imaging methods support normal cell divisions in explanted living brains over extended periods of over 30 hours of continuous high-quality 4D image acquisition, significantly extending what has previously been achieved (Cabernard & Doe, 2013). To analyse the resulting vast image data sets, we developed QBrain, an innovative, freely available, robust and easy to use machine learning based image analysis software. Using these tools, we characterised the *syp* mutant, showing a brain overgrowth phenotype that, surprisingly, is not due to an increase in the rate of NB division suggested by conventional analysis in fixed material. Instead, we show that brain overgrowth in *syp* mutants is due to an extension in the time over which NBs continue dividing. Our exemplar use of QBrain to characterise the *syp* mutant phenotype in the intact living larval brain, illustrates the power of our approach to quantitate the proliferation of individual cells in a large and complex tissue. We anticipate that QBrain could be applied effectively to many kinds of other complex tissues, such as normal or mutant mammalian embryoids or organoids, as well as many other *Drosophila* mutants.

RESULTS

An optimised approach for extended time-lapse imaging of developing *ex-vivo* brains

Drosophila larval brains develop for more than 120 hours (Homem & Knoblich, 2012) but imaging of live brain development at the cellular level has so far only been possible by imaging explanted brains for relatively short periods of a few hours (Cabernard & Doe, 2013; Prithviraj et al., 2012) or by studying disaggregated brain cells in culture (Homem *et al.,* 2013; Moraru *et al.,* 2012; Savoian & Rieder, 2002; Furst & Mahowald, *et al.,* 1985). To address this major technical gap, we modified the previous state-of-the-art methods of Cabernard & Doe (2013) to develop an easy, effective protocol for long-term culture and imaging of intact explanted larval brains for the analysis of stem-cell behaviour in whole-mounted living brains.

We first improved the isolation and culture of larval brains by combining gentle scissor-based dissection of second or third-instar larvae with an optimised culture medium and an improved brain mounting technique (Figure 1; Experimental Procedures). Second, we used bright, endogenously expressed protein traps Jupiter::GFP and Histone::RFP as markers of microtubules and chromosomes, respectively (Figure 1B). These provided sufficient information to identify cell types and follow their behaviour under live-imaging conditions with relatively low doses of excitation light. This allowed us to follow cell division in individual cells by imaging at subcellular resolution in 3D (Figure 1D). Generic cytological markers are more easily recognised across wild-type (WT) and different mutants than more specific markers, such as Deadpan (Dpn), Asense (Ase) or Prospero (Pros), commonly used to identify NBs, GMCs and progeny (Figure S2), but which are often disrupted in mutants. Finally, we optimised our imaging conditions using a standard commercial confocal microscope to reduce excitation light exposure while providing 3D data sets of sufficient temporal and spatial resolution to support analysis of cell proliferation over time (see Experimental Procedures).

To assess whether our culturing and imaging protocol supports normal development, we used a number of criteria. Overall, we found that by all the criteria we measured, brain development was normal in our *ex vivo* conditions. First, our brains generally did not show signs of damage during preparation, which can be easily seen as holes or lesions in the tissue that expand with time in culture. Second, our cultured larval brains consistently continue to develop and

increase in size (Figure 1C-C″). Finally, we do not observe significant lengthening or arrest of the cell cycle in NBs for 22 h, which is approximately the length of the wandering third instar larval stage (wL3) (Figure 1D-D'). With longer duration culture and imaging, up to 48 h, we observe an increase in cell cycle length, which might be expected for wL3 brains transitioning to the pupal state. NB division rates were 60-90 min per cycle for wL3, as previously published (Homem *et al*., 2013; Bowman *et al*., 2008; Figure 1D-D′; Movie S1 and S2). We conclude that our culturing and imaging method of intact explanted larval brains allows long term 3D imaging of development for at least 22h with sufficient time resolution to effectively track the cell cycle.

Easy automated quantification of cell types in an intact living brain

Progress in elucidating the molecular mechanisms of regulated cell proliferation during larval brain development has largely depended on the characterisation and quantification of mutant phenotypes by painstaking manual image analysis (Neumüller *et al.,* 2011). Our live cell 3D imaging in particular, results in datasets consisting of thousands of images. Analysing such large datasets manually is impractical, therefore, automating this process would be a significant advance (Rittscher, 2010). Although there are freely available image analysis tools, we find that none of those we tested for this kind of automated analysis perform adequately on our datasets, in terms of speed or accuracy (Table 1). To overcome this limitation, we developed QBrain, an easily deployed, machine learning based software. QBrain facilitates automated classification of cell types and quantitative analysis of cell number, distribution and proliferation from time-lapse movies of multichannel 3D image stacks of complex tissues (Figure 2; S1). In essence, the user "trains" QBrain by selecting a few examples of the cell type of interest and the program determines the pixel characteristics that identify that cell type, allowing subsequent characterisation of cell number, distribution and behaviour (see Supplemental Material for full description).

Ease of training is critical to the effective use of machine learning algorithms (Sommer & Gerlich, 2013). To minimise the supervision required of the user during the training process, we developed QBrain to use a novel implementation of supervised machine learning (see Experimental Procedures), in which the user trains the program in 2D on a limited number of images (Figure 2B). In practice, the user simply selects, with a single mouse click, the

approximate centre of all examples of a particular cell type within user-defined regions of interest in the image. This supervision approach is more convenient and faster than other machine learning based approaches, such as FIJI-WEKA (Arganda-Carreras *et al*., 2016) or Ilastik, (Sommer *et al*., 2011), that require extensive labelling of areas at the pixel level that include both cells and background (see Figure S1 for details of the user interface). During the learning of the model, QBrain chooses from a collection of filters and scores and combines them to find features in the image that identify the user-defined cell centres. In this way, a series of transformations of the image data (referred to as the "Trained Model") are learned. This model is applied pixel by pixel to further data sets, and QBrain then outputs both an estimated probability map of cell identification and the predicted cell centre co-ordinates. To optimise training, users can apply the probability map output to assess the accuracy of the prediction and if necessary, provide additional training (Fig 2B). This probability map and the predicted locations of cell centres across the entire volume and time-series are saved and can be passed to ImageJ (FIJI) for further manipulation (Figure 2B; S2). Thus, the program requires a minimal amount of manual user input to achieve accurate automated cell identification that is highly scalable to large image data sets.

In order to evaluate the performance of QBrain, we compared its output to "ground truth" data, in this case image sets that were manually annotated by a user. We first established and validated the algorithm on 3D images of fixed whole mounted (wL3) larval brains immuno-labelled against Ase and Dpn and including DAPI, which allowed definitive identification of NBs and GMC's (Neumüller *et al.,* 2011; Bayraktar *et al*., 2010; Boone & Doe, 2008). Dpn marks NBs uniquely, whereas Ase is expressed in NBs and in GMCs (Figure S2). We assessed the performance of the algorithm by plotting Precision-Recall graphs (Figure 3A; Davis & Goadrich, 2006) where optimum performance maximises the number of cells correctly identified (recall) while also maximising the accuracy of identification (precision). We used this analysis to explore parameters, such as the threshold setting, that affect algorithm performance, allowing us to decide which parameters should be fixed and which need to be user-modified (Figure 3A and Experimental Procedures). In particular, this approach allowed us to assess the level of training required to achieve good detection of cell types of interest with different datasets (Figure 3B). In all cases tested, we found that successful identification of NBs or GMCs required minimal user training (of the order of tens of

examples for only a few image planes) and increasing training gave only marginal improvement (Figure 3A; Figure S3). Taking our results so far, we conclude that our machine learning based approach performs accurate and efficient identification of cells from large multidimensional image sets of complex tissues.

We next determined how well QBrain performed cellular identification in the more challenging case of generic cytological markers. To assess whether QBrain can effectively identify the NBs and their progeny from generic markers, we fixed Jupiter::GFP / Histone::RFP expressing brains and labelled them for Dpn and Pros to identify NBs and their progeny (Figure 4A). After training, based only on the Jupiter::GFP / Histone::RFP labels, QBrain successfully and accurately identified both NBs (96% ± 4 Dpn positive, n = 12, 3 repeats) and progeny (92% ± 2 Pros positive, n = 189, 3 repeats) (Figure 4B-B″). We conclude that QBrain can be used effectively to identify NBs and progeny from either specific cell type markers or from generic markers of cell components that are expressed in all cells in the brain.

QBrain outperforms other automated analysis approaches

To assess and quantitate how QBrain analysis of complex multidimensional image data compares to other freely available programs (Table 1), we used our live-imaging time-series of the generic cytological markers Jupiter::GFP / Histone::RFP as standard test datasets. For our baseline performance tests of QBrain, we quantified the number of NBs identified in five time-points from a movie sequence. We then compared the output from QBrain to that of other algorithms applied to the same test dataset. In each case, we attempted to optimise the parameters used, based, whenever possible, on the published information. In our tests we found that QBrain significantly outperformed all the other freely available approaches in accuracy, speed and simplicity of use (Table 1). We conclude that QBrain represents a significant advance over the other current freely available state-of-the-art methods of analysis, especially in its ability to accurately and automatically analyse the large volumes of data that result from live imaging of an intact complex tissue such as a brain.

Analysis of *syp* mutants by QBrain highlights multiple subtle causes of brain over-growth

To test the power and versatility of using QBrain in the analysis of a complex and subtle brain mutant phenotype, we characterise the brain overgrowth phenotype of *syp* mutants. Syp has previously been identified in a screen for genes required for normal brain development (Neumüller *et al*., 2011), although the mutant was not characterised in detail. Therefore, we characterised the phenotype of mutant *syp* brains in greater detail using QBrain. We found that in early wL3, the brains of *syp* loss-of function mutants (eliminating Syp expression in the NB lineages, Figure S3) were significantly enlarged compared to WT larvae at the same stage of development. *syp* brain lobes exhibit a 23% increase in diameter (WT 206.5 µm ± 5.0, n = 10, *syp* 253.7 µm ± 11.0, n = 5), and a 35% increase in CB volume (Figure 5A-A″). We, first investigated whether our observed increase in volume was due to an increase in cell size. Using QBrain to locate cell centres within the CB region, we found that the average cell density is not significantly different between WT (104 cells/µm ± 12, n = 5) and *syp* mutants (92 cells/µm ± 4, n = 4), indicating no difference in average cell size (Figure 5B-B″). Given that cells were tightly packed in the CB and we did not observe substantial spacing (Figure 5B′), it follows that the increased area of the CB in *syp* mutants must contain more cells if cell density is not affected. We, therefore, conclude the larger CB region size must be explained by an increase in the number of cells.

Given this increase in the number of cells in the CB, we investigated possible causes. In *brain tumour* mutants, brain overgrowth is caused by additional ectopic NBs (Bello *et al*., 2006). We tested whether this is also the case for the *syp* mutant brains. We used QBrain to accurately determine the total number of NBs in the CB of fixed *syp* mutant verses WT wL3 brains. Our results show that wL3 *syp* Null brains have a small but statistically significant increase of 10-15% in the number of NBs of the dorsal anterior lateral region, but syp RNAi knockdown are not different from WT (Figure 6C; WT 45.6 ± 1.3, n = 22, RNAi 44.1 ± 2.1, n = 15, *syp* 51.7 ± 1.5, n = 15). This difference between *syp* RNAi and syp Null likely reflects a role of Syp in other tissues, or stages of development that impacts the regulation of NB number. We furthermore, did not observe any difference in the number of type II NB, normally 8 per brain lobe, located medially on the dorsal posterior (Fig S4; Ren et al., 2017; Bello *et al*., 2006; Boone & Doe, 2008; Bowman *et al*., 2008). We conclude that an increase in NB numbers in *syp* mutants does not quantitatively

account for the brain enlargement observed and further differences in cell proliferation must be contributing.

syp mutants exhibit a normal neuroblast division rate

In addition to increased NB number, an increase in the NB division rate during development would contribute significantly to brain overgrowth. To test this possibility, we examined the mitotic activity of NB in *syp* mutants by estimating NB division rate either through the uptake of 5-ethynyl-2 deoxyuridine (EdU) into progeny or by quantitating the number of cells in mitosis by the presence of Phospho-Histone H3 (PH3). Interestingly, these two independent methods gave conflicting results (Figure 5C, D). We found that the number of progeny produced in the 4 h EdU incubation period in *syp* Null larval brains is significantly increased compared to WT (Figure 5D). Surprisingly, PH3 staining show no significant difference in the NB mitotic index between *syp* Null, *syp* RNAi, and WT (Figure 5C-C′). As previously noted (Walker, 1954), mitotic index determination from fixed material relies on assumptions about the cell cycle, so even small changes can make the results hard to interpret.

In order to resolve these conflicting results, we determined the rate of NB division in cultured living brains using our optimised methods. Using QBrain and time-lapse imaging provides unequivocal characterisation of cell division in a brain, as it directly quantitates each NB's division rate individually (Figure 6B). We first validated that QBrain can automate the identification of individual dividing NB in WT from live image series (Figures 6A; S5). We then compared with *syp* mutants and found that the rate of division of NBs in *syp* mutant brains was not significantly different from WT (Figure 6B″). Interestingly, we also find that, while each NB has a consistent cycle period, there is considerable variation in cell cycle length between NB, however, there is no obvious spatial correlation of cell division rate (Figure S5) We conclude that mitotic activity of NB is unchanged in the absence of Syp expression and so does not contribute to the increased brain size at wL3. Nevertheless, these results illustrate the power of QBrain to analyse the pattern of cell divisions in much more detail and greater accuracy than conventional methods in fixed material.

syp mutant larvae develop more slowly causing brain overgrowth

So far, we have shown that an increase in NB numbers or their rate of proliferation does not explain the enlarged brains observed in *syp* mutant larvae. Another possible contributor to the enlarged brain phenotype could be that NBs divide for longer and produce more progeny. To test this possibility, we measured the time between embryo hatching and pupation in *syp* mutants compared with WT (Figure 6D). We found a significant developmental delay of approximately 50h for *syp* mutants to reach pupation (*syp* Null 170.5 ± 5.5, n = 4; *syp* RNAi 178.7 ± 19.0, n = 4) compared to WT (123.1 ± 2.2, n = 12). We conclude that a combined increase in NB numbers and developmental delay, prolonging the time over which NB generate progeny, accounts for the observed brain enlargement phenotype observed in wL3 *syp* mutant larvae.

Taken together our work demonstrates that QBrain is a powerful new analysis tool that transforms what is possible in the characterisation of mutant phenotypes at the level of individual cell behaviour in complex tissue in 3D. QBrain provides a simple, fast and effective approach for the analysis of subtle mutant phenotypes compared to existing automated methods or manual approaches. Our exemplar characterisation of *syp* mutant phenotypes illustrates the potential of QBrain to transform the analysis of developmental mutants, making it practical to work with very large 3D data sets of fixed material and 3D live-cell time-lapse imaging of complex intact tissues.

DISCUSSION

One of the great challenges in biology and biomedicine is to understand the development of the whole human brain at the single cell level, which is of major clinical significance (Dagley *et al*., 2017, Deistung *et al*., 2013). Whilst great strides have been made using isolated mammalian cells in culture and whole brain imaging using MRI approaches (Zorio *et al*., 2017; Ortega & Costa, 2016; Goense *et al*., 2016; Radecki *et al*., 2014; Deistung *et al*., 2013, Judenhofer *et al*., 2008), understanding developmental processes at the single cell level in the context of the whole brain is currently intractable in humans. Live-cell brain imaging *in vivo* is possible in rat and mouse model systems through cranial windows, for example, using multi-photon microscopes and Brainbow

technology (Mahou *et al*., 2012), however, the rodent brain is still too complex to follow overall development at the single cell level (Ortega & Costa., 2016; Weigert *et al*., 2013; Hoffman, 2008). Whole zebrafish (*Danio rario*) brains can be followed *in vivo* at the cellular level using light sheet microscopy (Araya *et al*., 2016; Dray *et al*., 2015; Babin *et al*., 2014; Schmidt, *et al.,* 2013; Keller *et al*., 2008), but the image resolution is insufficient to follow the intracellular molecular behaviour in detail. In contrast, *Drosophila* brains are tractable at the single cell level (Homem *et al*., 2015), and are sufficiently small to image the intracellular distribution of molecules at high resolution (Lemon *et al*., 2015; Cabernard & Doe, 2013; Homem *et al*., 2013; Prithviraj *et al.,* 2012) this makes them an appealing model system.

A generally applicable, automated analysis tool to assess tissue development

In *Drosophila* and vertebrates alike, progress in understanding brain development has been limited by the lack of effective ways to culture and image whole brains for extended periods, while monitoring cell behaviour with intracellular molecular discrimination. Here, we describe how we address this by making it possible to culture and image the intact living explanted *Drosophila* larval brain for extended periods at high resolution. In parallel, we developed QBrain, convenient and rapid software that uses a machine learning image analysis algorithm to identify neural stem cells and other cell types and quantitate their numbers, size and rate of division on an individual cell level from extensive complex datasets. The use of QBrain in this study illustrates how our approach could be used on any complex 4D data set, including time-lapse movies of vertebrate tissues, being limited only by the culturing and imaging techniques.

The key developments of our live imaging approach are firstly, the optimised dissection and mounting protocol, combined with simplified culture medium to extend the period of viability and mechanical stability of the specimens. Secondly, our use of very bright generic markers of cellular morphology, which offers major advantages over more specific markers of cell identity. Generic cytological markers tend to be brighter, allowing the use of low laser power to maximise viability. Markers of cell morphology can also be used in almost all mutant backgrounds, unlike specific markers of cell identity, whose expression is often altered in specific mutant backgrounds. Therefore, as we show, images of generic markers can be analysed regardless of the genetic background or conditions used to image the development of the tissue, offering a general

approach for most model organisms.

Our long term time-lapse experiments resulted in a huge volume of data, making manual image analysis impractical and certainly not scalable to include multiple conditions or genetic backgrounds, as discussed in Bria *et al*. (2016). The development of QBrain offers a generally applicable, automated analysis tool that can be applied to almost any equivalent kind of data sets in any organism. While a variety of powerful image analysis tools already exist and are in common use for handling 3D and 4D datasets (Luengo *et al*., 2017; Arganda-Carreras *et al*., 2016; Logan *et al*., 2016; Gertych, *et al*., 2015; Lou *et al*., 2014; Sommer *et al*., 2011), QBrain offers a simple solution for fast and accurate analysis of subtle phenotypic changes without the need for bespoke programming, script writing or optimisation of many parameters. Furthermore, while machine learning approaches are increasing in popularity (Chittajallu et al., 2015; Sommer & Gerlich, 2013), those currently freely available tend to be limited to the analysis of 2D data. Moreover, existing conventional tools that handle 3D datasets are often inflexible, expensive, hard to use or slow. We have demonstrated conclusively using detailed quantitative performance analysis in 4D that QBrain out-performs, by a significant margin, all the other freely available approaches that we tested. Our machine learning based approach, therefore, represents a step change in the scale of data sets that can be effectively analysed to obtain quantitative information on any user defined cell type, including changes in cell behaviour such as mitosis, cell number and size. Crucially, QBrain analysis of extensive live imaging data allows such parameters to be determined for individual cells in a complex tissue, rather than conventional methods that provide snapshots or an ensemble view of average cell behaviour.

Limitations

The approach we have developed depends critically on the use of “supervision” or training regimes, which by their very nature are subjective and user dependent. Supervised machine learning methods (Luengo *et al*., 2017; Arganda-Carreras *et al*., 2016; Logan *et al*., 2016; Chittajallu et al., 2015; Sommer *et al*., 2011) require the user to provide training examples by manually identifying a variety of cells or objects of interest, often requiring laborious “outlining” of features. However, our use of a “point and click” interface (Figure S1), which simplifies manual annotation, and probability maps, helps to overcome this drawback of many supervised machine

learning approaches by making it quick and easy for a user to train and retrain. Probability maps provide the flexibility for tailoring experimental design to produce robust and reproducible results with a minimal effort. Using our novel approach, a user can quickly move from initial observations to statistically significant results based upon bulk analysis of data. Currently, a technical limitation of the "point and click" strategy is that the program "assumes" a roughly spherical cell shape. This means that cellular projections, for example neural extensions, would not be identified. However, the output data from QBrain can be opened in other programs, such as FIJI (ImageJ), allowing a user to benefit from the many powerful plug in extensions available to facilitate further extraction of information for defined cell populations from bulk datasets. The combination of all these features make QBrain widely applicable to many kinds of complex datasets, fixed or live, where there is a need to identify, quantitate and analyse cell types and behaviours.

Quantitative analysis of developing brains at the cellular level elucidates subtle developmental defects

In our exemplar analysis of *syp* mutant brain overgrowth, we show how the powerful combination of our live imaging and detailed quantitative analysis by QBrain can be brought to bear to elucidate even a subtle complex mutant phenotype where conventional approaches struggle to produce a definitive result. In the case of the *syp* mutant phenotype, previous analysis identified an issue in cell proliferation (Neumüller *et al.,* 2011), however, using QBrain we reveal that the phenotype is more subtle and complicated than previously thought. Indeed, it has been shown that Syp has a large number of target genes so phenotypes might be expected to be complex (McDermott *et al*., 2014). By facilitating detailed analysis, increasing quantitative rigour and throughput to deal with appropriate numbers for statistical validity to tease out subtle affects, our approaches have significant implications for subsequent investigations of detailed molecular analysis to determine underlying molecular mechanisms. The use of bright generic cellular markers in conjunction with QBrain offers the potential to develop high throughput screening and data analysis for rapid and accurate identification of cell types in any complex tissue, for example applied to image data sets following cell fates in zebrafish labelled using the "spectrum of fates" approach (Araya *et al*., 2016; Chow *et al*., 2015; Almeida *et al*., 2014). Potential future applications could include high throughput

analysis of the effect of growth conditions on organoid development (Walsh *et al*., 2014) and drug discovery experiments using phenotypic characterisation of embryos or larvae rather than single cells (Willoughby *et al*., 2013; Rand *et al*., 2010).

AUTHOR CONTRIBUTIONS

MH, DW and LY contributed equally to this work. MH, LY, TJS, TD, YA and RMP designed and performed experiments and MH, LY, TJS, TD and RMP analysed and interpreted data. DW originated the computational approaches used and developed in collaboration with MH the software for 3D analysis in QBrain. MH extensively validated and tuned the software to the application of interest. LY initiated the project intellectually and the biological application. DW initiated the computational approaches used. All authors discussed the results and conclusions, commented on and contributed to the revision of the manuscript. RMP and ID supervised the project, the biological application and user interface as well as jointly writing and revising the manuscript.

ACKNOWLEDGEMENTS

We are grateful to: Ivo A. Telley (Instituto Gulbenkian de Ciência) for fly stocks; David Ish-Horowicz and Alfredo Castello for discussions and critical reading of the manuscript. Thanks to MICRON (http://micronoxford.com, supported by a Wellcome Strategic Awards 091911/B/10/Z and 107457/Z/15/Z) for access to equipment and assistance with imaging techniques. This work was supported by: a Clarendon Fellowship (Oxford University Press) to L.Y.; MRC/BBSRC/EPSRC (grant number MR/K01577X/1) and the Wolfson Foundation, Medical Research Council (MRC) Grants MC_UU_12010/Unit Programs G0902418 & MC_UU_12025 supporting D.W.; Wellcome Trust Senior Research Fellowship (081858) to I.D. and supporting R.M.P; Wellcome Trust Four-Year PhD Studentship (105363/Z/14/Z) to T.J.S. and by funding from the Engineering and Physical Sciences Research Council (EPSRC) and Medical Research Council (MRC) [grant number EP/L016052/1] supporting M.H.

REFERENCES

Almeida, A. D., Boije, H., Chow, R. W., He, J., Tham, J., Suzuki, S. C. & Harris, W. A. (2014). Spectrum of Fates: a new approach to the study of the developing zebrafish retina. Development, *141*, 1971–1980.

Araya, C., Carmona-Fontaine, C. & Clarke, J. D. W. (2016). Extracellular matrix couples the convergence movements of mesoderm and neural plate during the early stages of neurulation. Dev Dyn *245*, 580–589.

Arganda-Carreras *et al*. (2016). https://zenodo.org/record/59290#.WFrLF2Wh3dQ
FIJI-WEKA

Babin, P. J., Goizet, C. & Raldúa, D. (2014). Zebrafish models of human motor neuron diseases: advantages and limitations. Progress in Neurobiology, *118*, 36–58.

Barbosa & Ninkovic (2016). Adult neural stem cell behavior underlying constitutive and restorative neurogenesis in zebrafish. Neurogenesis, *3:1*, e1148101.

Bello, B., Reichert, H. & Hirth, F. (2006). The brain tumor gene negatively regulates neural progenitor cell proliferation in the larval central brain of *Drosophila*. Development *133*, 2639–2648.

Berger, C., Harzer, H., Burkard, T. R., Steinmann, J., van der Horst, S., Laurenson, A.-S., Novatchkova, M., Reichert, H. & Knoblich, J. A. (2012). FACS purification and transcriptome analysis of *Drosophila* neural stem cells reveals a role for Klumpfuss in self-renewal. Cell Reports, *2*, 407–418.

Boone, J. Q. & Doe, C. Q. (2008). Identification of *Drosophila* type II neuroblast lineages containing transit amplifying ganglion mother cells. *Developmental Neurobiology*, *68*, 1185–1195.

Bowman, S. K., Rolland, V., Betschinger, J., Kinsey, K. A., Emery, G. & Knoblich, J. A.(2008). The tumor suppressors Brat and Numb regulate transit-amplifying neuroblast lineages in *Drosophila*. Developmental Cell *14*, 535–546.

Breiman, L. (2001). Random forests. Machine learning *45*, 5–32.

Breiman, L., Friedman, J., Stone, C.J., & Olshen, R.A. (1984). Classification and regression trees. CRC press, Taylor and Francis group. ISBN 9780412048418

Bria, A., Iannello, G., Onofri, L. & Peng, H. (2016) 'TeraFly: real-time three-dimensional visualization and annotation of terabytes of multidimensional volumetric images.', Nature Methods *13*, 192–194.

Cabernard, C. & Doe, C. Q. (2013). Live imaging of neuroblast lineages within intact larval brains in *Drosophila*. Cold Spring Harbor Protocols *10*, 970–977.

Caussinus, E., & Gonzalez, C. (2005). Induction of tumor growth by altered stem-cell asymmetric division in *Drosophila melanogaster*. Nature Genetics, *37*, 1125–1129.

Chia, W., Somers, W. G. & Wang, H. (2008) *Drosophila* neuroblast asymmetric divisions: cell cycle regulators, asymmetric protein localization, and tumorigenesis. *J Cell Biol 180*, 267–272.
Chow, R. W., Almeida, A. D., Randlett, O., Norden, C. & Harris, W. A. (2015). Inhibitory neuron migration and IPL formation in the developing zebrafish retina. Development *142*, 2665–2677.

Chittajallu, D.R., Florian, S., Kohler, R.H., Iwamoto, Y., Orth, J.D., Weissleder, R., Danuser, G. & Mitchison, T.J.(2015). In vivo cell-cycle profiling in xenograft tumors by quantitative intravital microscopy. Nat Methods 12, 577–585.

Dagley, A., LaPoint, M., Huijbers, W., Hedden, T., McLaren, D. G., Chatwal, J. P., Papp, K. V., Amariglio, R. E., Blacker, D., Rentz, D. M., et al., (2017) 'Harvard Aging Brain Study: Dataset and accessibility.', NeuroImage *144*, 255–258.

Davis, J. & Goadrich, M. (2006). The Relationship Between Precision-Recall and ROC Curves. Proceedings of the 23rd International Conference on Machine Learning, Pittsburg, PA.

Deistung, A., Schäfer, A., Schweser, F., Biedermann, U., Güllmar, D., Trampel, R., Turner, R. & Reichenbach, J.R. (2013). High-Resolution MR Imaging of the Human Brainstem In vivo at 7 Tesla. Front. Hum. Neurosci. *7*, 710.

Dray, N., Bedu, S., Vuillemin, N., Alunni, A., Coolen, M., Krecsmarik, M., Supatto, W., Beaurepaire, E. & Bally-Cuif, L.(2015). Large-scale live imaging of adult neural stem cells in their endogenous niche. Development *142*, 3592–3600.

Fiaschi L., Koethe, U., Nair, R. & Hamprecht, F.A. (2012). Learning to count with regression forest and structured labels. IEEE 1st International Conference on Pattern Recognition (ICPR), 2685–2688.

Fiji (ImageJ V1.51d; http://fiji.sc)
FIJI - local threshold (http://imagej.net/Auto_Local_Threshold)

Furst, A. & Mahowald, A. P. (1985). Cell division cycle of cultured neural precursor cells from *Drosophila*. Developmental Biology *112*, 467–476.

Gao, Y. & Kilfoil, M.L., (2009). Accurate detection and complete tracking of large populations of features in three dimensions. Opt Express 17, 4685–4704.

Gertych, A., Ma, Z., Tajbakhsh, J., Velásquez-Vacca, A. & Knudsen, B. S. (2015) 'Rapid 3-D delineation of cell nuclei for high-content screening platforms.', Computers in biology and medicine. doi: 10.1016/j.compbiomed.2015.04.025.

Geurts, P., Ernst, D. & Wehenkel, L. (2006). Extremely Randomized Trees. Machine Learning, *63*, 3-42.

Goense, J., Bohraus, Y. & Logothetis, N. K. (2016). fMRI at High Spatial Resolution: Implications for BOLD-Models. Front Comput. Neurosci. *10*, 66.

Graeden, E. & Sive, H. (2009). Live Imaging of the Zebrafish Embryonic Brain by Confocal Microscopy. J. Vis. Exp. *26*, e1217.

Halstead J.M., Lin Y.Q., Durraine L., Hamilton R.S., Ball G., Neely G.G., Bellen H.J. & Davis I. (2014) Syncrip/hnRNP Q influences synaptic transmission and regulates BMP signaling at the *Drosophila* neuromuscular synapse. Biol. Open. 3, 839-49.

Hoffman, R. M. (2008). Imaging In Mice With Fluorescent Proteins: From Macro To Subcellular. Sensors, *8*, 1157–1173.

Homem, C. C. F., & Knoblich, J. A. (2012). *Drosophila* neuroblasts: a model for stem cell biology. Development *139*, 4297–4310.

Homem, C. C. F., Reichardt, I., Berger, C., Lendl, T., & Knoblich, J. A. (2013). Long-term live cell imaging and automated 4D analysis of *Drosophila* neuroblast lineages. PLoS ONE *8*, e79588.

Homem, C. C. F., Steinmann, V., Burkard, T. R., Jais, A., Esterbauer, H. & Knoblich, J. A. (2014). Ecdysone and mediator change energy metabolism to terminate proliferation in Drosophila neural stem cells. Cell *158*, 874–888.

Homem, C. C. F., Repic, M., & Knoblich, J. A. (2015). Proliferation control in neural stem and progenitor cells. Nature Reviews Neuroscience, *16*, 647–659.

Judenhofer, M. S., Wehrl, H. F., Newport, D. F., Catana, C., Siegel, S. B., Becker, M., Thielscher, A., Kneilling, M., Lichy, M. P., Eichner, M., Klingel, K., Reischl, G., Widmaier, S., Röcken, M., Nutt, R. E., Machulla, H.-J., Uludag, K., Cherry, S. R., Claussen, C. D. & Pichler, B. J. (2008). Simultaneous PET-MRI: a new approach for functional and morphological imaging. Nat. Med. *14*, 459–465.

Keller, P. J., Schmidt, A. D., Wittbrodt, J. & Stelzer, E. H. (2008). 'Reconstruction of Zebrafish Early Embryonic Development by Scanned Light Sheet Microscopy', Science *322*, 1065–1069.

Kohwi, M. & Doe, C. Q. (2013). Temporal fate specification and neural progenitor competence during development. Nature Reviews Neuroscience *14*, 823–838.

Laurenson, A.-S., Saini, N. & Reichert, H. (2013). Targeted Transgenic RNAi Knockdown of Cell Fate Determinants Induces Neoplastic Tumor Growth and Metastasis in a Drosophila Transplantation Model of Neural Stem Cell Derived Cancer. J Stem Cell Res Ther S12. doi: 10.4172/2157-7633.S12-002

Lemon, W. C., Pulver, S. R., Höckendorf, B., McDole, K., Branson, K., Freeman, J. & Keller, P. J. (2015). Whole-central nervous system functional imaging in larval *Drosophila*.. Nature communications *6*, 7924-7940.

Lempitsky, V. & Zisserman, A. (2010). "Learning to count objects in images". Conference Report: Advances in Neural Information Processing Systems, 1324–1332.

Li, X., Chen, Z., & Desplan, C. (2013). Temporal patterning of neural progenitors in *Drosophila*. Current Topics in Developmental Biology *105*, 69–96.

Lindeberg, T. (1994). Scale-Space Theory in Computer Vision.
Springer. ISBN 0-7923-9418-6.

Liu, Z., Yang, C.-P., Sugino, K., Fu, C.-C., Liu, L.-Y., Yao, X., Lee, L.P. & Lee, T., (2015). Opposing intrinsic temporal gradients guide neural stem cell production of varied neuronal fates. Science *350*, 317–320.

Logan D.J., Shan J., Bhatia S.N. and Carpenter A.E. (2016). Quantifying co-cultured cell phenotypes in high-throughput using pixel-based classification. Methods, *96*, 6–11.

Lou, X., Kang, M., Xenopoulos, P., Muñoz-Descalzo, S., & Hadjantonakis, A.-K. (2014). A rapid and efficient 2D/3D nuclear segmentation method for analysis of early mouse embryo and stem cell image data. Stem Cell Reports, *2*, 382–397.

Luengo, I., Darrow, M.C., Spink, M.C., Sun, Y., Dai, W., He, C.Y., Chiu, W., Pridmore, T., Ashton, A.W., Duke, E.M.H., Basham, M. & French, A.P. (2017). SuRVoS: Super-Region Volume Segmentation workbench. J Struct Biol, *198*, 43–53.

Mahou, P., Zimmerley, M., Loulier, K., Matho, K.S., Labroille, G., Morin, X., Supatto, W., Livet, J., Débarre, D. & Beaurepaire, E. (2012). Multicolor two-photon tissue imaging by wavelength mixing. Nat Methods, *9*, 815–818.

Medioni, C., Ephrussi A. & Besse, F. (2015). Live imaging of axonal transport in *Drosophila* pupal brain explants. Nature Protocols, *10*, 574–584.

Meijering, E. (2012). IEEE Xplore Abstract - Cell Segmentation: 50 Years Down the Road [Life Sciences]. Signal Processing Magazine.

Meijering, E., Dzyubachyk, O., & Smal, I. (2012). Methods for cell and particle tracking. Methods in Enzymology, *504*, 183–200.

Mcdermott, S.M., Meignin, C., Rappsilber, J. & Davis, I. (2012). *Drosophila* Syncrip binds the gurken mRNA localisation signal and regulates localised transcripts during axis specification. Biology Open, 1, 488–497.

McDermott, S.M., Yang, L., Halstead, J.M., Hamilton, R.S., Meignin, C. & Davis, I. (2014). *Drosophila* Syncrip modulates the expression of mRNAs encoding key synaptic proteins required for morphology at the neuromuscular junction. RNA, *20*, 1-14.

Miles, W. O., Dyson, N. J., & Walker, J. A. (2011). Modeling tumor invasion and metastasis in *Drosophila.* Disease Models & Mechanisms, *4*, 753–761.

Moraru, M.M., Egger, B., Bao, D.B., & Sprecher, S.G. (2012). Analysis of cell identity, morphology, apoptosis and mitotic activity in a primary neural cell culture system in *Drosophila*. *Neural* Development, *7*, 1-10.

Myers, G. (2012). Why bioimage informatics matters. Nature Methods, *9*, 659–660.

Narbonne-Reveau, K., Lanet, E., Dillard, C., Foppolo, S., Chen, C.H., Parrinello, H., Rialle, S., Sokol, N.S & Maurange, C. (2016). Neural stem cell-encoded temporal patterning delineates an early window of malignant susceptibility in *Drosophila*. eLife *2016; 5*:e13463

Neumüller, R. A., Richter, C., Fischer, A., Novatchkova, M., Neumüller, K. G., & Knoblich, J. A. (2011). Genome-wide analysis of self-renewal in *Drosophila* neural stem cells by transgenic RNAi. Cell Stem Cell, *8*, 580–593.

Ortega, F. & Costa, M. R. (2016). Live Imaging of Adult Neural Stem Cells in Rodents. Front Neurosci, *10*, 78.

Patton, E. E. & Zon, L. I. (2001).The art and design of genetic screens: zebrafish. Nat Rev Genet, *2*, 956–966.

Perrimon, N., Ni, J.-Q. & Perkins, L. (2010). In vivo RNAi: today and tomorrow. Cold Spring Harb Perspect Biol, *2*, a003640.

Prithviraj, R., Trunova, S. & Giniger, E. (2012). Ex vivo culturing of whole, developing *Drosophila* brains. JOVE: 65.

Rabinovich, D., Mayseless, O. & Schuldiner, O. (2015). Long term ex vivo culturing of *Drosophila* brain as a method to live image pupal brains: insights into the cellular mechanisms of neuronal remodeling. Front. Cell. Neurosci *9*, (2015).

Radecki, G., Nargeot, R., Jelescu, I. O., Le Bihan, D. & Ciobanu, L. (2014). Functional magnetic resonance microscopy at single-cell resolution in Aplysia californica. Proc Natl Acad Sci USA *111,* 8667–8672.

Rand, M. D., Kearney, A. L., Dao, J. & Clason, T. (2010). Permeabilization of *Drosophila* embryos for introduction of small molecules. Insect Biochem. Mol. Biol. *40*, 792–804.

Ren Q., Yang C., Liu Z., Sugino K., Mok K., He Y., Ito M., Nern A., Otsuna H. & Lee T. (2017) Stem Cell-Intrinsic, Seven-up-Triggered Temporal Factor Gradients Diversify Intermediate Neural Progenitors. Curr. Biol. *27,* 1303-1313.

Rittscher, J. (2010). Characterization of biological processes through automated image analysis. Annual Review of Biomedical Engineering, *12*, 315–344.

Savoian, M. S. & Rieder, C. L. (2002). Mitosis in primary cultures of *Drosophila* melanogaster larval neuroblasts. Journal of Cell Science, *115,* 3061–3072.

Schmidt, R., Strähle, U. & Scholpp, S. (2013). Neurogenesis in zebrafish – from embryo to adult. Neural development 8, 1-13.

Schmitz, C., Eastwood, B. S., Tappan, S. J., Glaser, J. R., Peterson, D. A. & Hof, P. R. (2014). Current automated 3D cell detection methods are not a suitable replacement for manual stereologic cell counting. Frontiers in Neuroanatomy, *8*, 1-13.

Scott, E. K. & Baier, H. (2009). The cellular architecture of the larval zebrafish tectum, as revealed by gal4 enhancer trap lines. Frontiers in Neural Circuits, *3*, 1-14.

Sommer, C. & Gerlich, D.W. (2013). Machine learning in cell biology - teaching computers to recognize phenotypes. J Cell Sci 126, 5529–5539.

Sommer, C., Straehle, C., Kothe, U. & Hamprecht, F.A. (2011). Ilastik: Interactive learning and segmentation toolkit, in:. Presented at the 2011 8th IEEE International Symposium on Biomedical Imaging (ISBI 2011), IEEE, pp. 230–233. doi:10.1109/ISBI.2011.5872394

Waithe, D., Hailstone, M., Lalwani, M.K., Parton, R.M., Yang, L., Patient, R., Eggeling, C. &Davis, I. (2016). "3-D Density Kernel Estimation for Counting in Microscopy Image Volumes using 3-D Image Filters and Random Decision Trees", Computer Vision – ECCV 2016 Workshops, *10*, 244-255.

Walker, P. (1954). The mitotic index and interphase processes. J Exp Biol *31*, 8-15.

Walsh, A.J., Cook, R.S., Sanders, M.E., Aurisicchio, L., Ciliberto, G., Arteaga C. L. & Skala M.C. (2014). Quantitative optical imaging of primary tumor organoid metabolism predicts drug response in breast cancer. Cancer Research *74*, 5184–5194.

Weigert, R., Porat-Shliom, N. & Amornphimoltham, P. (2013). Imaging cell biology in live animals: ready for prime time. J Cell Biol *201*, 969–979.

Willoughby, L.F., Schlosser, T., Manning, S.A., Parisot, J.P., Street, I.P., Richardson, H.E., Humbert, P.O. & Brumby, A.M. (2013). An *in vivo* large-scale chemical screening platform using *Drosophila* for anti-cancer drug discovery. Disease Models & Mechanisms *6*, 521–529.
Wu, J. S. & Luo, L. (2006). A protocol for dissecting *Drosophila melanogaster* brains for live imaging or immunostaining. Nature protocols *1*, 2110–2115.

Zorio, D. A. R., Jackson, C. M., Liu, Y., Rubel, E. W. & Wang, Y. (2017). Cellular distribution of the fragile X mental retardation protein in the mouse brain. J. Comp. Neurol. *525*, 818–849.

FIGURES AND TABLES

Fig.1: Extended 3D time-lapse imaging of live *ex-vivo* cultured brains

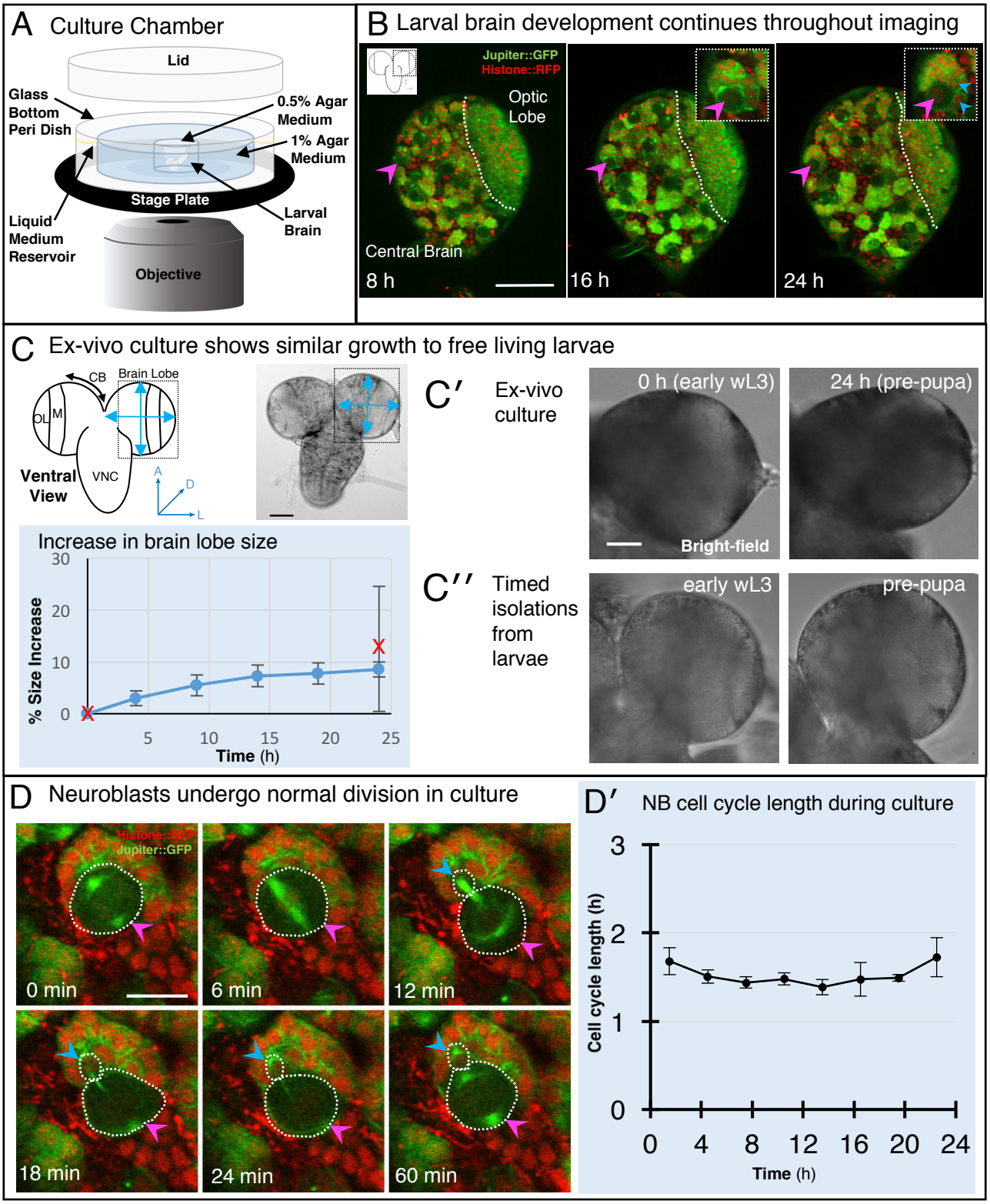

Figure 1. Extended 3D time-lapse imaging of live *ex-vivo* cultured brains. **A**) Diagram of the chamber and sample preparation for long-term time-lapse imaging on an inverted microscope (see Experimental Procedures). **B**) 24 h, confocal 3D time-lapse imaging of a developing larval brain lobe (see insert diagrams) labelled with Jupiter::GFP and Histone::RFP. Images were aligned across time by reference features to take account of movements and shape changes. Arrowheads indicate NBs (magenta) and progeny (cyan); a dashed white line indicates the boundary to the medulla. The insert reference diagram, top left, and corresponding reference map in (**C**), show the orientation and region of the brain imaged. **C**) Plot of brain lobe diameter growth over 24 h (n = 3) under wide-field fluorescence imaging conditions in culture for a Jupiter::GFP; Histone::RFP L3 brain. The red crosses indicate average lobe diameter (n= 13) for freshly isolated brains from free living larvae at the wL3 and pre-pupal stages; inserts diagram the brain orientation and region of the brain imaged. **C′)** and **C″)**, bright field images at two time-points during culture and examples of freshly dissected free living larvae at corresponding developmental stages, respectively. **D**) An individual dividing NB from a confocal time-lapse image sequence of the brain lobe. **D′**) Plot of cell cycle length over time in culture for cultured L3 brains showing that cell cycle length for NB does not lengthen significantly over at least 20h under imaging conditions. Scale bars **B, C′ D″** 50 μm; **C** 100 μm; D 10 μm.

Fig.2 QBrain analysis workflow

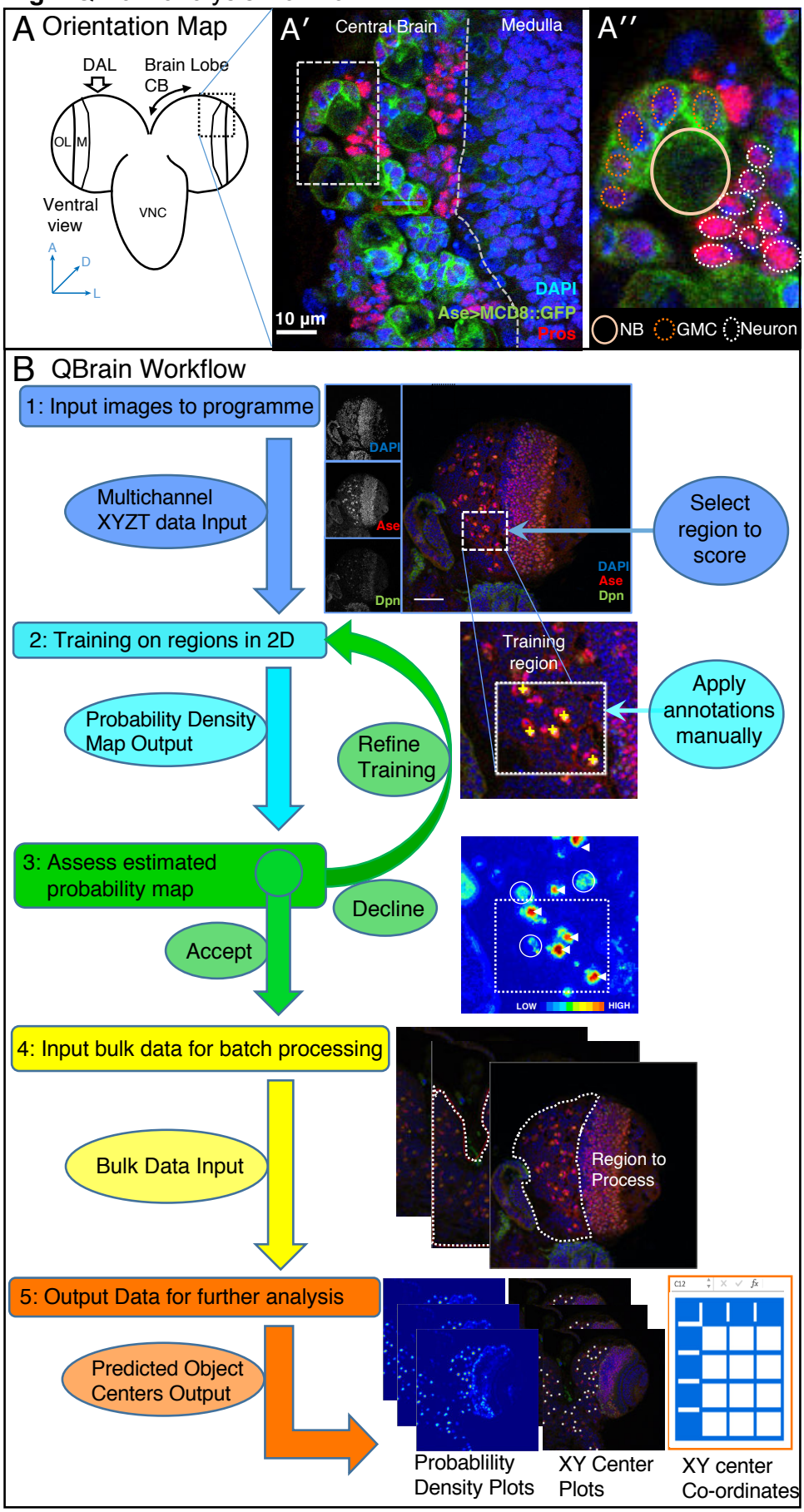

Figure 2. QBrain analysis workflow. **A**) Overviews of the wL3 brain highlighting the dorso-anterior-lateral region of the CB containing cells of the type I NB lineage; OL optic lobe; M medulla; VNC ventral nerve chord; DAL dorsal anterior lateral. **A′**) Confocal image of the CB region with the type I NB lineage identified in fixed material by DAPI, *Ase*-Gal4 driving UAS mCD8::GFP and anti-Pros immuno-labelling. **A″**) Enlarged region of (**A**) showing a single NB lineage; NB neuroblast; GMC ganglion mother cell. **B**) Workflow for automated identification of cell types by QBrain. Refer to the Main Text and Methods for details. Briefly, training is performed by single click annotation within a user defined region of interest (ROI) to identify the cell class of interest. The resultant "probability" map for cell class identification is evaluated manually to assess the success of training. A successful identification regime / "Model" is saved and may be used to batch process multiple image data sets. Multiple outputs are produced including a list of the co-ordinates of identified cells. Multiple identification regimes can be sequentially applied to identify multiple cell classes from a single data set.

Fig. 3: Validation of neuroblast identification by QBrain

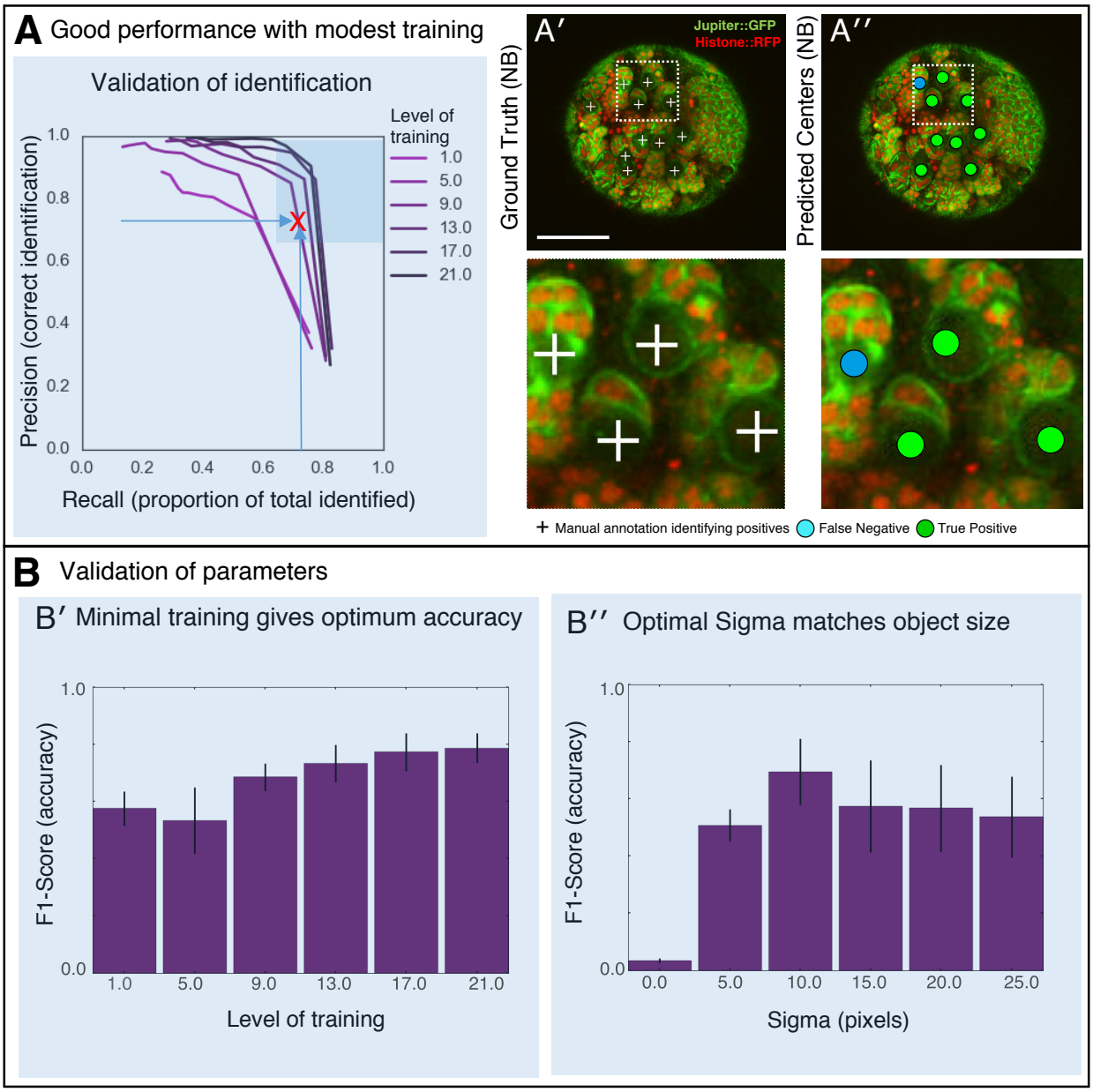

Figure 3. Validation of neuroblast identification by QBrain. **A**) Assessment of algorithm performance in identifying NB from confocal image data of a live brain labelled with Jupiter::GFP, Histone::RFP. The Precision-Recall (P/R) relationship (see main text) was plotted for different levels of training from annotation of one cell (NB), to annotations of 21 individual NB. The dark blue shaded area highlights the optimum performance of precision and recall; the X corresponds to the image data in (**A′**) and (**A″**). **A′**) Ground Truth manual identification of NB centres. **A″**) Corresponding identifications (green markers) and "misses" (cyan markers) for the point on the P/R curve (**A**) corresponding to 70% precision and recall, marked with a red cross. Zoomed regions correspond to the white dashed regions in the main image. Scale bars 50 μm. **B**) Validation of parameters: **B′**) assessing level of training (Number of NB identifications) required for optimum detection accuracy at the default threshold of 0.05; **B″**) The value of sigma (~object size in pixels) required for optimal detection accuracy at the default threshold value, 0.05. Near-optimal performance is achieved at a range of sigma values.

Fig. 4: Accurate automated identification of cell classes from generic labels

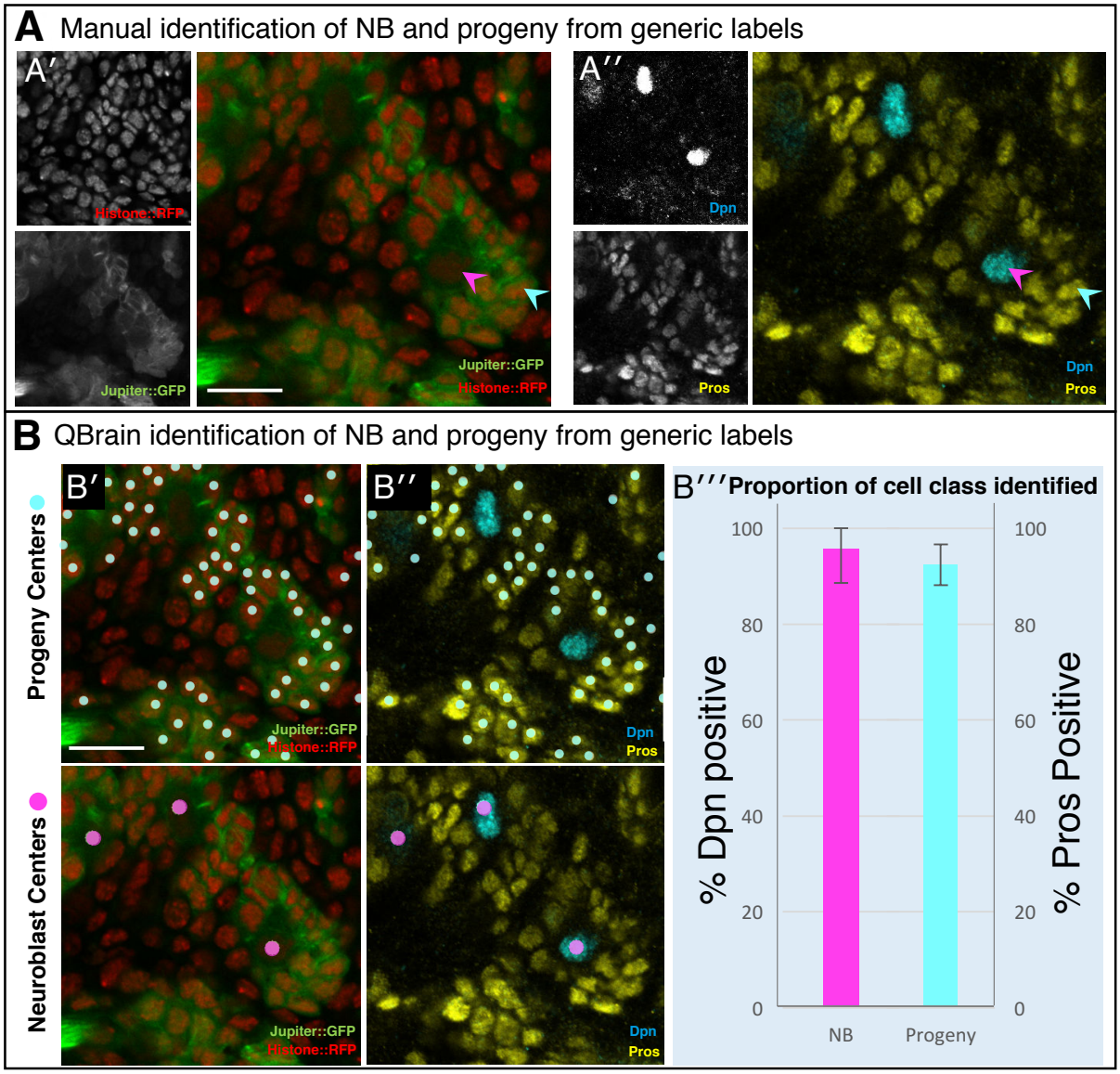

Figure 4. Accurate automated identification of cell classes from generic labels. **A**) A fixed Jupiter::GFP, Histone::RFP labelled brain (**A′**), immuno-labelled for Dpn and Pros (**A″**) to permit unequivocal identification of NB and their progeny. **B**) Validation of QBrain identification of NB and progeny from generic cytological makers. **B′**) Cell centre predictions are shown from QBrain analysis of the dataset from (**A′**) with generic markers. **B″**) Corresponding identifications of NB and progeny based upon Dpn and Pros markers. **B‴**) Plot showing that identification based upon Jupiter::GFP, Histone::RFP labelling alone effectively identifies NB and progeny compared to identification from Dpn and Pros labels: 96% ± 4 NB identification (n=12, 3 repeats) and 92% ± 2 progeny identification (n=189, 3 repeats). Scale bars 20 μm.

TABLE 1: QBrain outperforms other freely available programs for cell class identification

	Fiji/auto local threshold	Fiji/Weka	Ilastik (1.17)	QBrain V0.1	Manual
Total Parameters to select	1	25	67	6	-
Handles 3-D easily	YES	YES	YES	YES	-
Handles 4-D easily	NO	NO	YES	YES	-
Time to Train model (min.)	N/A	18	15	6	-
Post processing required?	YES	YES	INCLUDED	INCLUDED	-
Time to Run (min. including postprocessing)	5	105	70	19	550 (equivalent)
% True Positive	N/A	63.5±10.0	68.6±3.4	94.2±3.3	-
% False Negative	N/A	36.5±10.0	31.3±3.4	5.8±3.3	-
% False Positive	N/A	38.5±13.3	11.8±3.4	1.9±5.8	-
Success?	FAIL	PARTIAL	PARTIAL	EXCELLENT	-

Table 1. QBrain out-performs other freely available programs for cell class identification. Performance for a series of freely available tools for identifying cells was tested and compared to QBrain on the same computer, including time taken to provide user annotations for a standard data set (150 or 35 time-points, 30-Z). Computer specifications: MacBook Pro11,5; Intel Core i7 2.88GHz;16GB RAM. For manual annotations, the time taken to annotate the full dataset was estimated from the time to annotate 10 time-points. Only freely available approaches capable of analysing data in 4D were tested. Values ± standard deviations are shown, n=3. Fiji, ImageJ V1.51d; FIJI, local threshold V1.16.4; FIJI-WEKA, WEKA3.2.1; Ilastik (V1.17).

Fig.5: Brain lobe enlargement in *syp* mutant wL3 larvae

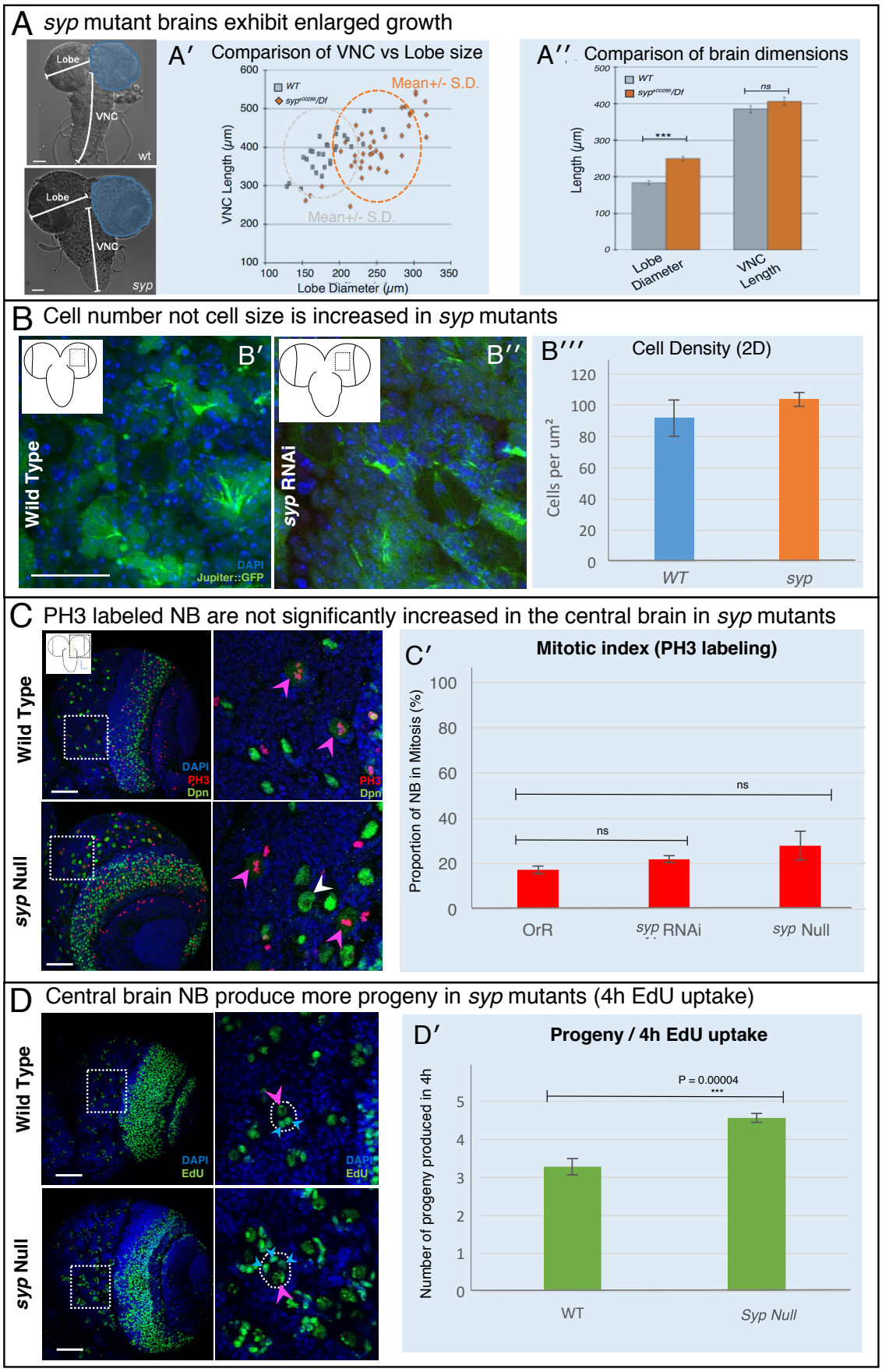

Figure 5. Brain lobe enlargement in syp mutant wL3 larvae. **A**) *syp* mutants have significantly enlarged brains compared to WT, at wL3. **A′-A″**) Comparison of brain dimensions for WT and *syp* mutants highlighting enlargement of the brain lobes. **B**) Average cell size is not increased in the CB region of *syp* mutants: **B′-B″**) cells are similarly tightly packed in both WT and *syp* RNAi CB; **B‴**) there is no difference in cell density between WT and *syp* mutants indicating cell size is unchanged. **C**) Mitotic index determination for CB NB by PH3 labelling shows no significant increase in the rate of division of *syp* mutants compared to WT. **C′**) Histogram comparing mitotic index: WT 17 +/- 8 (n = 21); *syp* RNAi 22 +/- 6 (n = 15); *syp* Null 21 +/- 6 (n = 15). Images show a typical PH3 labelling, zoomed regions correspond to the white dashed areas in the main image; Dpn and DAPI permit NB identification. **D**) Central brain NB produce significantly more progeny in *syp* mutants than WT by EdU uptake. Images show a typical EdU uptake, all progeny produced within the 4h period are labelled, zoomed regions correspond to the white dashed areas in the main image; a single NB and progeny are highlighted with a white dashed line. **D′**) Histogram comparing numbers of progeny produced: WT 3.3 +/- 0.2 (n=7); *syp* Null 4.6+/- 0.1 (n=7). Magenta arrows: NB; cyan arrowheads: progeny. Scale bars 20 μm in **B**; 50 μm elsewhere.

Fig. 6: Multiple factors lead to central brain enlargement in *syp* mutants

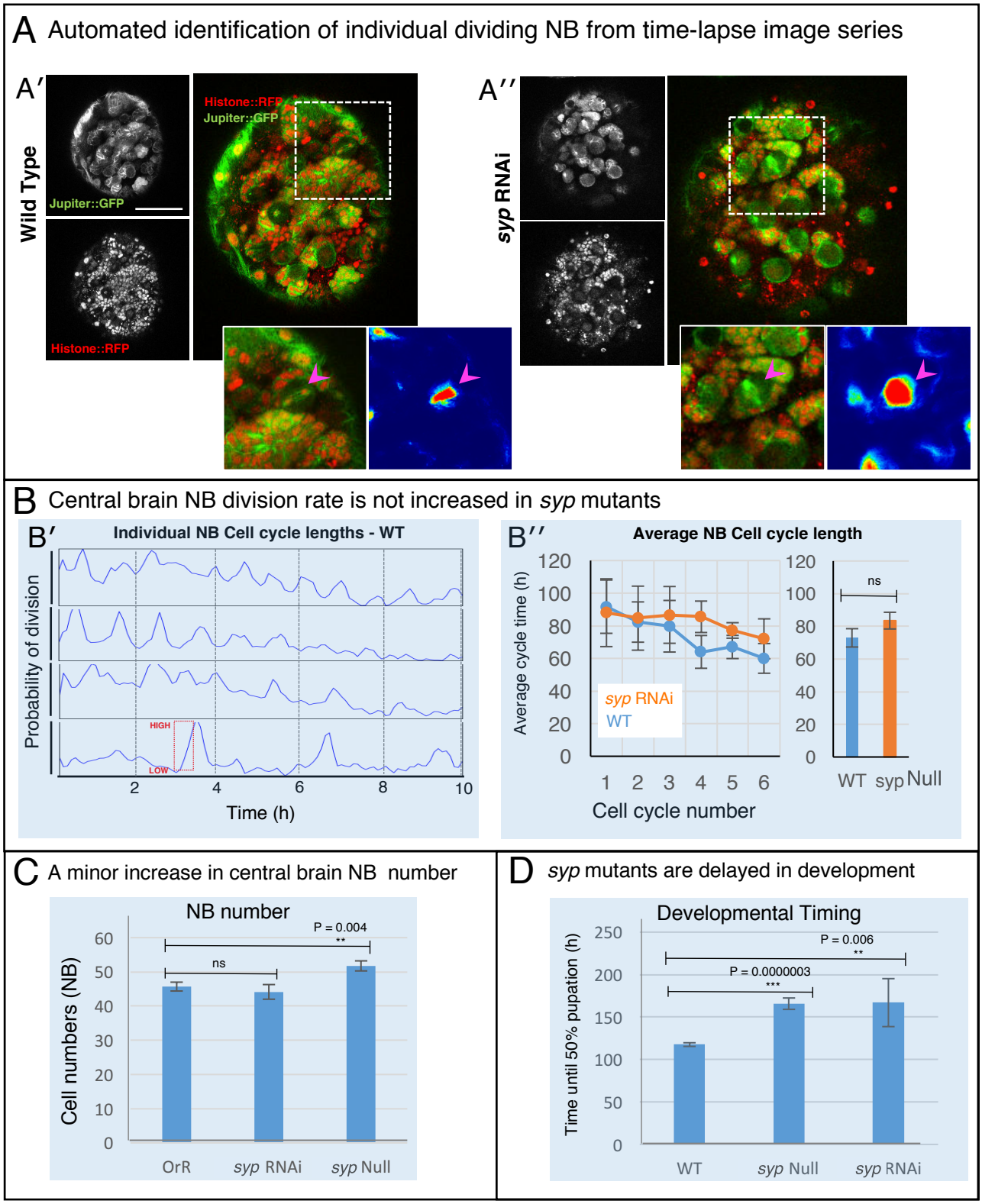

Figure 6. Multiple factors lead to central brain enlargement in *syp* mutants **A**) Automated identification of dividing NB using QBrain. (**A′-A″**) Raw image data and cell centre predictions are shown for single time-points from live, 3D time-lapse, confocal image data sets (imaged at one Z-stack / 10 min); magenta arrowheads indicate dividing NBs. **B**) Analysis of individual NB behaviour in the intact brain. **B′**) Variation in cell cycle length for four individual NB in a single WT brain see Figure S5). **B″**) The average cell-cycle time does not differ significantly between the *syp* RNAi and WT, indicating that there is no difference in the mitotic index of NB; average cycle time is plotted for consecutive cell cycles and as a mean cycle time (n=8). **C**) *syp* Null mutants, but not *syp* RNAi, show a small but significant increase in NB number (WT 45.6 ± 1.3 n = 22,; RNAi 44.1 ± 2.1 n = 15; *syp* 51.7 ± 1.5 n = 15). NB were identified by Dpn labelling and the average count for a comparable volume of a single optic lobe CB region is plotted. **D**) *syp* mutants are delayed in development compared to WT at the same time after embryo hatching (*syp* Null 170.5 ± 5.5 n = 4; *syp* RNAi 178.7 ± 19.0 n = 4; WT 123.1 ± 2.2 n = 12). Scale bar 50 μm.

EXPERIMENTAL PROCEDURES

EXPERIMENTAL MODEL AND SUBJECT DETAILS

Fly strains

Stocks were raised on standard cornmeal-agar medium at either 21 ºC or 25 ºC. To assist in determining larval age, Bromophenol Blue was added at 0.05% final concentration in cornmeal-agar medium. The following *Drosophila* fly strains were used: [Wild-Type Oregon-R]; [Jupiter::GFP;Histone::RFP (recombination on the third)]; [AseGal4>UAS-MCD8-GFP]; [w^{11180};PBac(PB)*syp*^{e00286}/TM6B]; [Bloomington 9289, w^{11180} (homozygote *syp* Null)]; [Df(3R)BSC124/TM6B (crossed to BL 9289 for *syp* Null)]; [*syp* RNAi lines - w^{11180}; P{GD9477} v33011, v33012].

METHOD DETAILS

Fixed Tissue Preparation and labelling

Flies of both genders were raised as described above and larvae from second instar to pre-pupal stages collected and dissected directly into fresh 4 % EM grade paraformaldehyde solution (from a 16 % stock. Polysciences) in PBS with 0.3 % TritonX-100 then incubated for 25 min at room temperature (RT). Following fixation, samples were washed 3 times for 15 min each in 0.3 % PBST (1x PBS containing 0.3 % Tween) and blocked for 1 h at RT in Immunofluorescence blocking buffer (1 % BSA prepared in 0.3% PBST). Samples were incubated with primary antibody prepared in blocking buffer for either 3 h at RT or overnight at 4˚C. Subsequently, samples were washed 3 times for 20 min each with 0.3 % PBST followed by incubation with fluorescent labelled secondary antibodies prepared in

blocking buffer for 1 h at RT. For nuclear staining, DAPI was included in the second last wash. Samples were mounted in VECTASHIELD (Vector Laboratories) for examination.

Culture of live explanted larval brains on the microscope

Brains were dissected from 3rd instar larvae in Schneider's medium according to https://www.youtube.com/watch?v=9WIloxxFuy0 and placed inside the wells of a pre-prepared culturing chamber (Figure 1A). To assemble the culturing chamber, 1 % low melting point (LMP) agarose (ThermoFischer) was prepared as 1:1 v/v ratio of 1 x PBS and Schneider's medium (ThermoFisher 21720024) then pipetted onto a 3 cm Petri dish (MatTek) dish and allowed to solidify. After solidification, circular wells were cut out using a glass capillary ~ 2 mm diameter. To secure the material in place, a 0.5 % LMP solution [1 % LMP solution brain diluted 1:1 with culturing medium (BCM)] was pipetted into the wells to form a cap. Finally, the whole chamber was flooded with BCM. BCM was prepared by homogenising ten 3rd instar larvae in 200 µl of Schneider's medium and briefly centrifuge to separate from the larval carcasses. This lysate was added to 10 ml of 80 % Schneider's medium, 20 % Fetal Bovine Serum (GibcoTM ThermoFisher), 10 µl of 10 mg/ml insulin (Sigma). A lid is used to reduce evaporation.

Imaging

Confocal, live imaging was performed using either an inverted Olympus FV1200 six laser line spectral confocal with environmental chamber, fitted with high sensitivity gallium arsenide phosphide (GaAsP detectors), x60 1.4 NA, or x60 SI 1.3 NA lenses. The confocal pinhole was set to one airy unit to optimise optical sectioning with emission collection. Laser power was kept less than ~4 µW for both 488 nm and 559 nm excitation. Images were collected at 1024x124 pixels (pixel size 0.207 µm) with a scan dwell time of 2.0 µs/pixel (frame rate 6.5 s/frame, averaged x2). The total exposure time per Z stack (35) frames was 3 min, 48 s. Alternatively a GE Deltavision Core widefield system was used with a Lumencor 7-line illumination source. For live culture and imaging the culturing chamber containing the sample was closed with a lid was kept at 20 °C inside the microscope environmental chamber. For imaging of fixed material, either an Olympus

FV1200 or FV1000 confocal was used with x20 0.75 dry or x60 1.4 NA. lenses. Settings were adjusted according to the labelling and were kept consistent within experiments.

Image Analysis

All programs used for image analysis were installed on a MacBook Pro11,5; Intel Core i7 2.88GHz; 16GB RAM. Basic image handling and processing was carried out in FIJI (ImageJ V1.51d; http://fiji.sc). The QBrain software was written in Python and can be installed as a stand-alone program. A full install is available (www.GitHub.com/dwaithe).

Western blot

Five wL3 brains of each genotype were dissected in Schneider medium and homogenised in 20 ul of lysis buffer (50 mM Tris-HCl pH 8.0, 150 mM NaCl, 0.5 % NP-40, 10 % glycerol, 1 mini tablet of Complete EDTA-free protease inhibitor). Proteins were separated by SDS-PAGE on a NuPage 4-12 % Novex Bis-Tris gradient gel (invitrogen) then transferred to nitrocellulose membrane with the Trans-Blot Turbo Transfer System (BioRad) following the manufacturer's protocol. Membranes were blocked in 50 % Blocking Buffer (Odyssey) in 0.3 % PBST for 1 h at room temperature. The membrane was incubated with α-Syp antibody [guinea pig, 1:2000, (McDermott *et al*. 2014)], and α-Tubulin antibody (mouse, 1:500, Sigma) overnight at 4°C. After rinsing, the membrane was incubated with secondary antibodies for LICOR (1:2000) for 2 h at room temperature. Membranes were washed and the protein bands were visualised with the quantitative infrared imaging system (LI-COR Odyssey, LI-COR Biosciences; Lincoln, NE).

QUANTIFICATION AND STATISTICAL ANALYSIS

Mutant comparisons were performed using Student's T test, following Shapiro-Wilk test to test normal distribution of the data. A p-value of <0.05 was considered significant.Numbers of replicates are detailed in the figure legends and main text. Unless otherwise stated, error bars shown are standard error (SEM).

DATA AND SOFTWARE AVAILABILITY

The following freely available image analysis tools were used: Fiji, ImageJ V1.51d (http://fiji.sc); Ilastik (V1.17) (http://ilastik.org; Logan *et al*., 2016; Sommer *et al*., 2011). The QBrain software was written in Python and can be installed as a stand-alone program. A full install is available (www.GitHub.com/dwaithe).

KEY RESOURCES TABLE

REAGENT or RESOURCE	SOURCE	IDENTIFIER
Antibodies		
Guinea pig anti-Syncrip (use 1:100)	I.Davis Lab (McDermott *et al.* 2012)	N/A
Mouse anti-Prospero (use 1:100)	Abcam	ab196361
Guinea pig anti-Asense (use 1:200)	Gift from JA Knoblich	N/A
Rat anti-Deadpan (use 1:100)	Abcam	ab195173
Goat anti-Mouse Alexa Fluor 488 (use 1:250)	ThermoFischer	A-11001
Goat anti-Guinea Pig Alexa Fluor 647 (use 1:250)	ThermoFischer	A-21450
Goat anti-Rabbit Alexa Fluor 594 (use 1:250)	ThermoFischer	R37117
Goat anti-Mouse Alexa Fluor 647 (use 1:250)	ThermoFischer	A-32728
Chemicals, Peptides, and Recombinant Proteins		
VECTASHIELD Antifade Mounting Medium	VECTOR Laboratories	H-1000
Formaldehyde, 16%, methanol free, Ultra Pure	Polysciences, Inc.	18814-20
Low melting point agarose	ThermoFischer	
Foetal Bovine Serum (BSA)	GibcoTM, ThermoFischer	
Schnider's Medium	ThermoFischer	21720024
Bromophenol Blue	Sigma-Aldrich	116K3528
Deposited Data		
Experimental Models: Organisms/Strains		
Drosophila: Wild-Type, Oregon-R	Bloomington	2376
Drosophila: Jupiter::GFP, Histone::RFP (recombined on the third)	Ephrussi Lab	
Drosophila: AseGal4>>UAS-MCD8-GFP		

Drosophila: w^{11180};PBac(PB)*syp*^{e00286}/TM6B		
Drosophila: w[11180]; Df(3R)BSC124/TM6B	Bloomington	9289
Drosophila:*syp* RNAi lines w^{11180}; P{GD9477}v33011, v33012		
Drosophila: ase-GAL4	Gift from JA Knoblich	N/A
Software and Algorithms		
Fiji, ImageJ (V1.51d)	Schindelin *et al.* 2012	*http://imagej.nih.gov/ij*
Ilastik (V1.17)	Sommer, C; Straehle C; Koethe U; Hamprecht FA (2011)	ilastik.org
QBrain	This article	This article
SoftWoRx, Resolve3D	GE Healthcare	N/A
Microsoft Excel	Microsoft Cooperation	150722
Other		
Superfine Vannas dissecting scissors	WPI	501778
MatTek (or Eppendorf) 3 cm glass-bottom Petri- dish	MatTek (or Eppendorf)	P35G-1.5-14-C

SUPPLEMENTAL INFORMATION

Application of an ensemble of decision trees framework to identify and quantitate cell classes in 4D

With the development of QBrain, we aim to make identification of cell types in multi-dimensional image sets as straightforward as possible. We do so by asking the user to identify cell centres for a small number of 2D image slices. From this information, an ensemble of decision trees model is 'learned' that is able to predict the cell centres in 2D. We can then infer the location of cell centres in 3D, by applying a 3D filter, which enhances the detections and resolves their coordinates in the additional dimension. Using the cell centre annotation and the estimated size of the cells, we create an initial 'probability map' of cell centres, similar in concept to density kernel estimation approaches (Waithe, *et al*., 2016, Fiaschi *et al*., 2012, Lempitsky & Zisserman, 2010). We then apply a series of image filters, which pull out image features such as edges, and try to use these features to predict a new probability map of cell centres. We generate this new probability map using a machine learning algorithm known as a "ensemble of decision trees" (Breiman, 2001; Breiman *et al*., 1984), which creates a series of "decision trees" that individually predict poorly, but averaged together are a strong predictor. Once we have the new probability map, we can apply another filter, in 3D that combines information from all the 2D slices and predicts the new cell centres. Through filtering this probabilistic interpretation of the image in 3D we are able to identify cells of interest. Such techniques are more powerful than simple segmentation approaches because they amalgamate feature-based information, encoding detail about the local neighbourhood, rather than just relying on the intensity information at each pixel.

The QBrain software has three main components in its workflow: The 2D training and evaluation algorithm, the 3D object finding algorithm and the 3D ROI drawing and interpolation algorithms. The software is written in python and includes a Graphical User Interface (GUI) written using PyQt library. The 2D training and evaluation algorithm utilises an ensemble of random decision trees and a bank of filters which utilise the sklearn, vigra and scipy python libraries. For the 2D training and evaluation algorithm the user must provide some images and some annotation

indicating the location of objects or cells within regions of an image. The user annotates 2-D sections of the 3D image volumes and defines the rectangular regions which encapsulate areas containing cells or just background. There are N image volumes ($I_{i=1}$, I_2, I_3,…, I_N) in the training set and M annotation sections where M > 1 ($A_{j=1}$, A_2, A_3,…, A_M). Each annotation contains a region of interest ($R_{j=1}$, R_2, R_3,…, R_M) and also a set of corresponding points ($P_{j=1}$, P_2, P_3,…,P_M) with one or more dot/points Pj = {$pt_{c=1}$, pt_2,…,pt_C} or no points if the region only contains background. As the model is designed to distinguish cells from the background it maybe appropriate to annotate regions as empty so as to acclimatise the model to the background. The points and regions are supplied by the user as they label the centroid locations of cells or objects within the image plane of interest. For each annotation we produce a centre-of-mass probabilistic representation ($F_{j=1}$,F_2, F_3…,F_M) which for each pixel (p) is defined as the minimum value of all the Gaussian kernels centred on dot annotations which overlap this pixel:

$$\forall p \in R_j, F_j^0(p) = max\left[\mathcal{N}\left(p; pt, \sigma^2 \mathbf{1_{2x2}}\right)\right], \forall pt \in P_j$$

and σ = [σ_x, σ_y]. The kernel is isotropic ($\sigma_x = \sigma_y$) as long the cells of interest are roughly spherical which is usually the case. For this application we recommend choosing a sigma which is smaller the radius of the cells. The Gaussian will weight pixels in the centre of cells more highly than those towards the edges or in the background. Finding the maximum pixel, rather than summing pixels amongst all the overlapping Gaussians we ensure that pixels at the edges of objects, but overlapping, are not more highly weighted than pixels that are central and represent the centre of the cells.

For each pixel in the annotation region we calculate a feature vector which describes the corresponding image pixels. Each descriptor of the feature vector is created through processing of the input image or volume with one of a bank of filters which included: Gaussian, magnitude of Gaussian, Laplacian of Gaussian, minimum and maxiumum eigenvalues of curvature (Fiaschi *et al*., 2012). These filter kernels are applied at multiple scales (sigma = 0.8, 1.6, 3.2 and 6.4) to aggregate data from the surrounding pixels into the feature descriptor at that specific pixel. This scale range was appropriate for all the cases used in this study and were not changed.

Once training data has been supplied by the user and the pixel features calculated, an ensemble of random decision trees is used to learn the association between input pixels and the centre-of-mass probabilistic representation (Geurts *et al*., 2006). The decision tree framework was parameterised as follows: the data was sampled at a rate of 1/200 from the input regions, with 30 trees generated during training, with a depth of 20 levels and a minimum split condition of 20 samples for each node. At each node 7 features were considered. Once trained, the decision tree framework can be applied to unseen images (without user annotation), requiring only input features to be calculated. Evaluation of images produces a probabilistic representation of where the cell centres are located, highly similar to the representation used during training.

The 3D object finding algorithm is applied to the output images of the random decision tree framework and involves multiple steps. Firstly the output images of the decision framework are rearranged into a 3D volume, this provides a representation of the probability of cell centres in 3D. To facilitate the object identification we next apply a determinant of hessian blob detector which smooths our signal and also enhances objects of a specific size (Lindeberg, 1994). Using this filter greatly simplifies our cell identification procedure although some idea of the size of the object is required $h = [h_x, h_y , h_z]$ (where $h_x = h_y$ if the object is spherical in two dimensions and $h_x = h_y = h_z$ if the object is spherical in three dimensions). Finally a 3D maxima finding algorithm is used to identify the centroid locations of the enhanced objects present in hessian filtered image (Gao and Kilfoil, 2009). For this a simple threshold either fixed or as a percentage of the maximum peak intensity is used.

To allow for selective application of the 3D counting algorithm in regions of a brain over time a novel Region Of Interest (ROI) interpolation algorithm was introduced. The user defines a ROI by clicking points around an area of interest in a single image (e.g. top of brain region). The user then defines another region either at the other end of the object (e.g. bottom of brain region) or partially through the region. The algorithm can then interpolate between these user-defined ROI to create a ROI for each frame in the image-volume. The User can then repeat this process in subsequent time-frames, and the algorithm will interpolate the ROI between frames creating a smooth transition which can be tweaked through the addition of further user defined regions to smoothly follow a 3D region of the brain over time. The interpolation is performed using bilinear

interpolation of points sampled uniformly along the user defined ROI. Objects or cells with a centroid position within the brain region can then be filtered from the image volume allowing for selective counting and location of cells over-time within a specific brain region.

SUPPLEMENTAL FIGURES

Fig. S1: QBrain graphical user interface

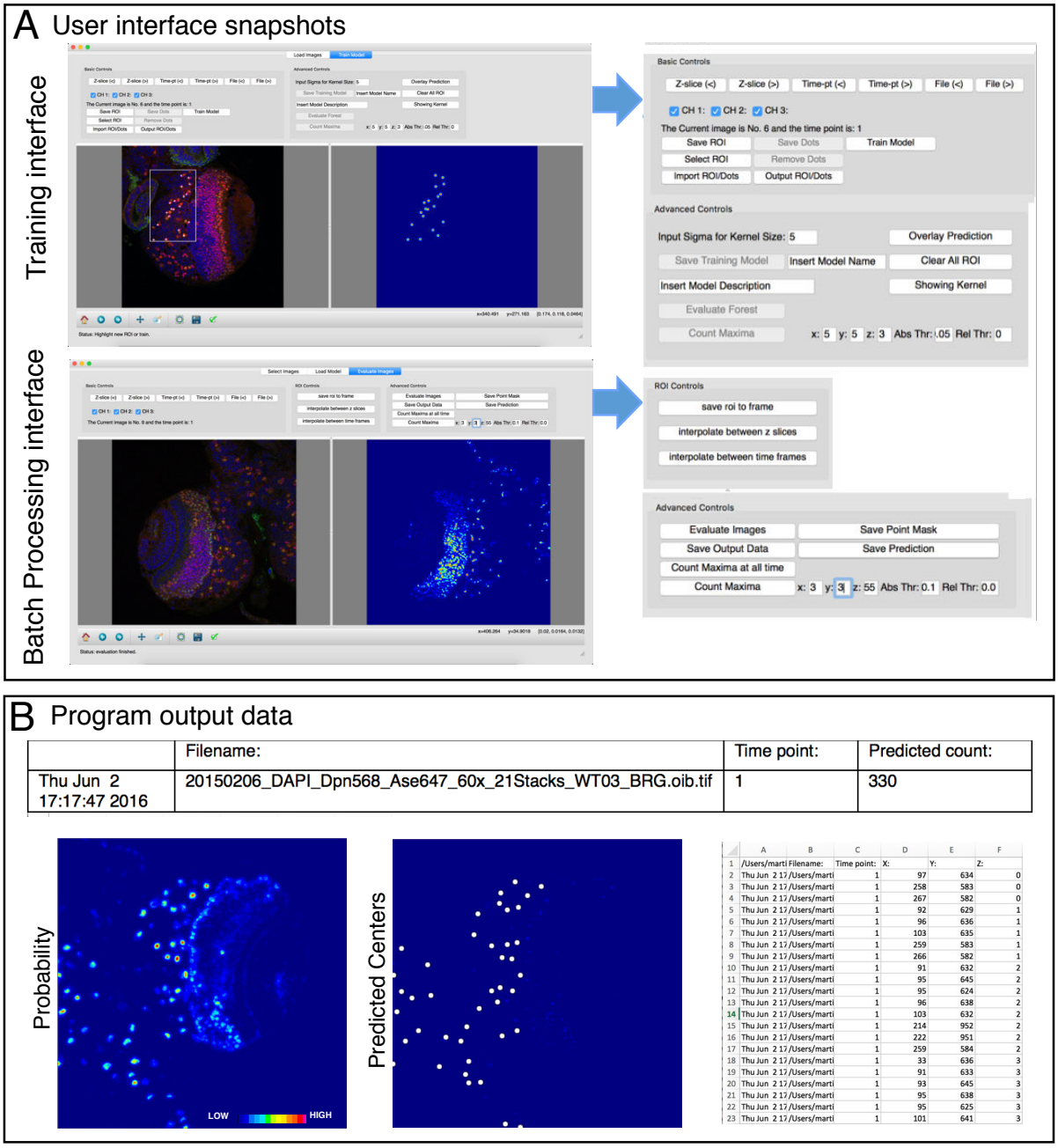

Figure S1. QBrain graphical user interface. **A**) Snapshot of the user interface for training (above) and batch processing (below), with the user defined settings enlarged to the right (see Supplementary Materials and Methods). (**B**) Output results summary for automated detection of a cell class: count; probability map, predicted centres overlay; XY co-ordinates for predicted centres.

Fig. S2: QBrain identification of cell types

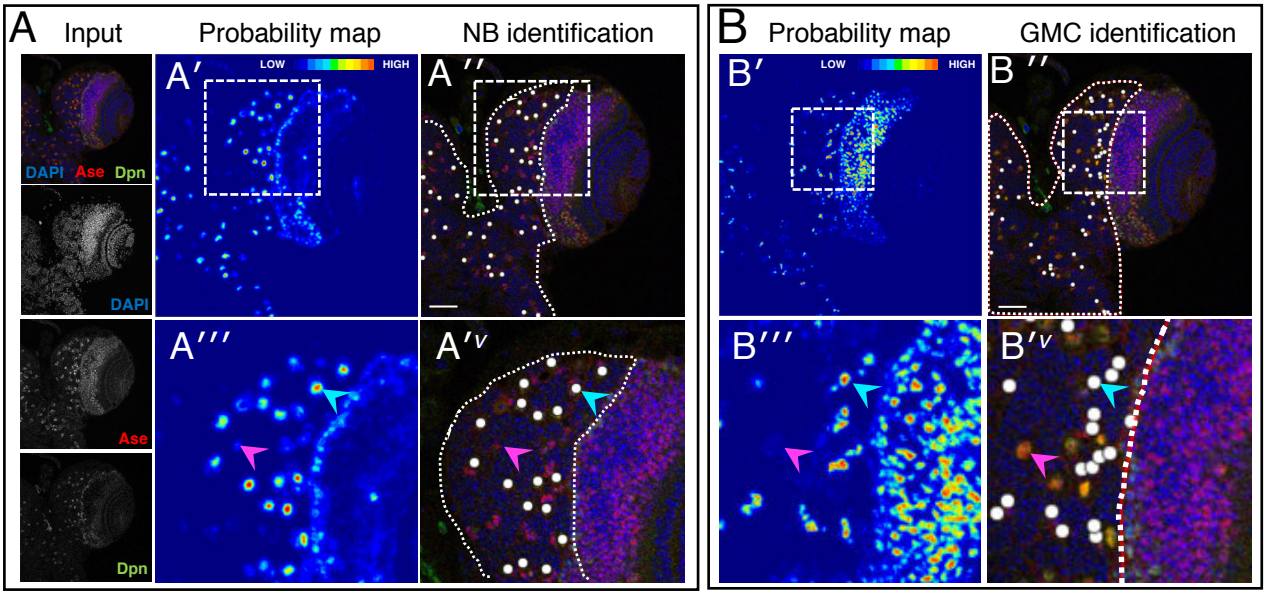

Figure S2. QBrain identification of cell types. Examples of automated detection of **A**) Type-I NBs and **B**) GMCs, respectively, from a 3D multichannel image set for a fixed WT larval brain labelled with DAPI, anti-Ase and anti-Dpn. In both cases training was performed by single click annotation within a user defined region of interest (ROI, dotted lines in **A″** and **B″**) to identify the cell class of interest. The resultant "probability" maps and corresponding cell class identifications (e.g. **A′** and **A′**) were evaluated manually to assess the success of training. The zoomed regions (corresponding to the dashed white boxes) show examples of correct identification (cyan arrowheads) and false negative (magenta arrowheads) of NB in **A′**^{v}) and GMC's in **B′**^{v}). Scale bars 50 μm.

Fig. S3: Syp is absent from mutant brains

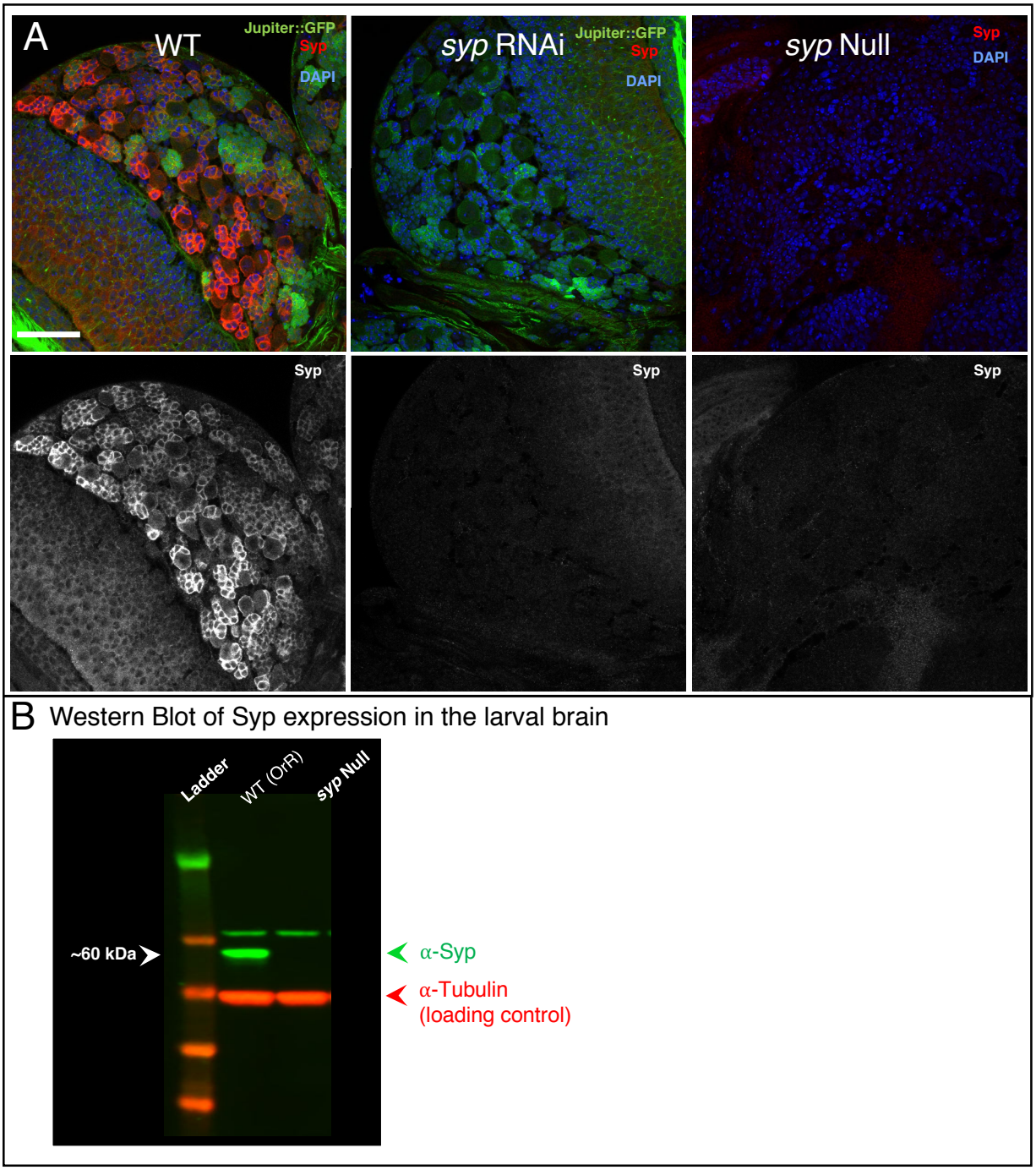

Figure S3. Syp is absent from syp Null and in *syp* RNAi larvae. **A**) Immunofluorescence analysis of Syp expression levels in WT, *syp* RNAi, and *syp* mutant CB. **B**) Western blot showing the complete absence of the major isoform of Syp from brain tissue of the *syp* Null line. Note the remaining band is a background band from the antibody. Scale bar 25 μm.

Fig. S4: Type II NB proliferation is unaffected in the *syp* mutant wL3 brain

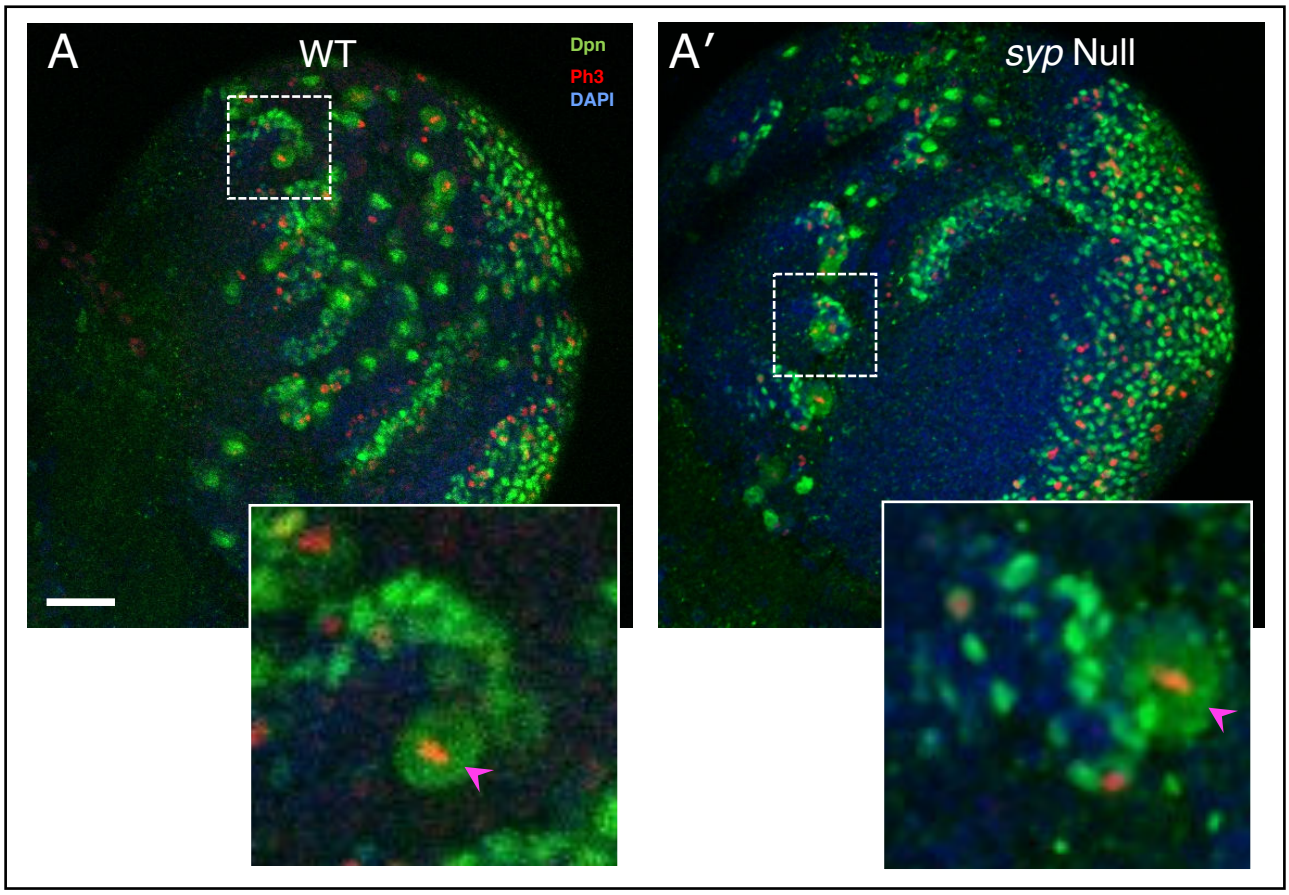

Figure S4. Type II NB proliferation is unaffected in the *syp* mutant wL3 brain. A-A′) View of type-II NB on the dorsomedial posterior brain surface comparing WT and *syp* mutant brains. Inserts show an individual type-II NB niche, magenta arrowheads identify the NB. No difference in NB numbers were observed. Scale bar 40 μm.

Fig. S5: Direct analysis of NB division from time-lapse imaging of live brains

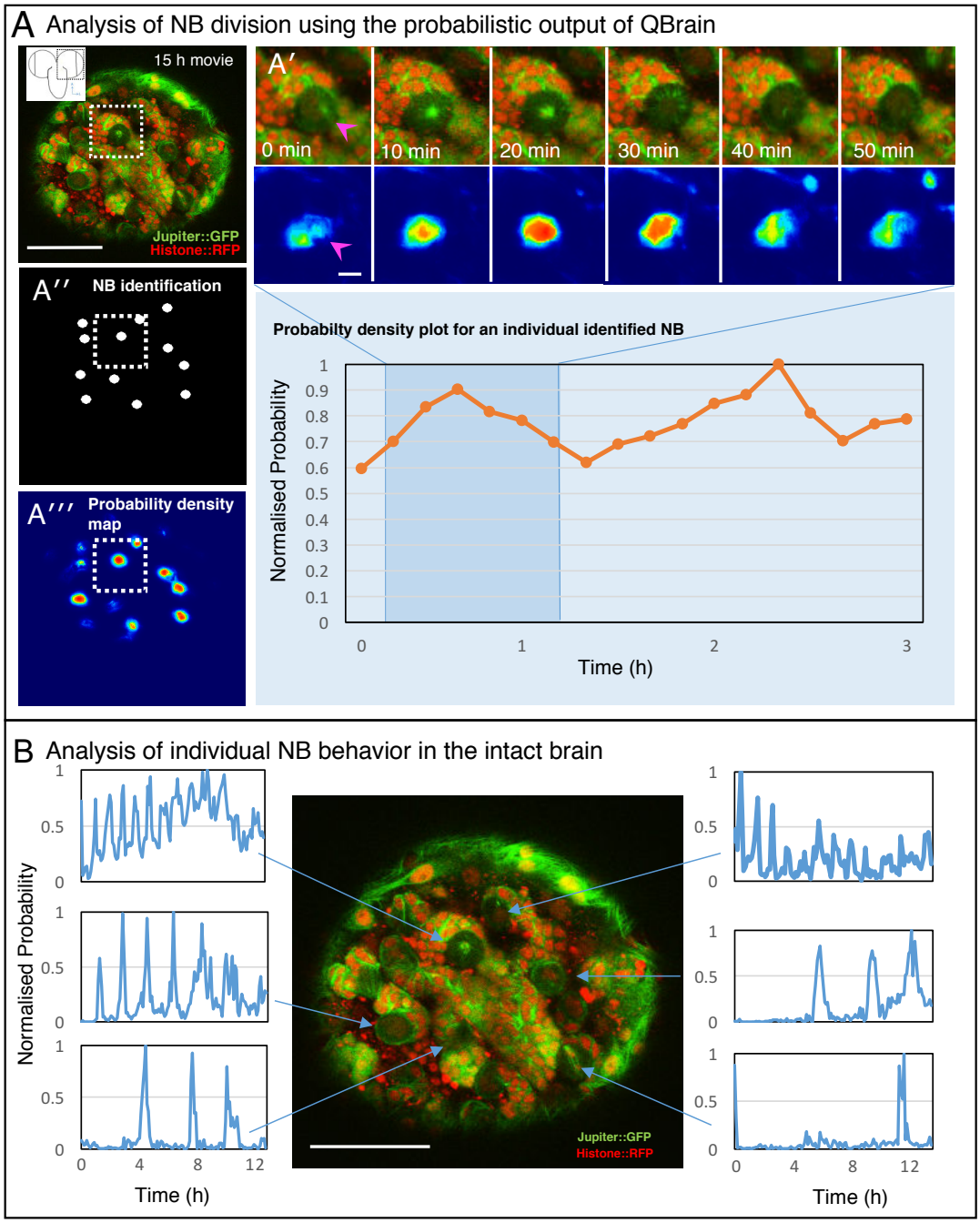

Figure S5. Direct analysis of NB division from time-lapse imaging of live explanted larval brains. **A-A′′′**) Using the probability density map output of QBrain, individual NBs can be followed through their cell cycle. **A′**) shows an individual NB and the corresponding Probability Density Map output plotted over time for that NB. **A′′**) Predicted centres of NBs and **A′′′**) the corresponding probability density map. **B**) Analysis of cell cycle over time for individual NBs mapped to their location in the CB, six examples are shown. Scale bar 40 µm.

SUPPLEMENTAL MOVIES

Supplemental Movie 1: (See Figure 1B) Development of a live explanted larval brain under extended time-lapse imaging conditions. Time-series (13h) of one of the brain lobes, collected at 6 minute intervals and displayed at 3 fps. Red: Histone::RFP; Green: Jupiter::GFP. Asymmetric division of a NB regenerates a daughter NB and produces a smaller GMC. Scale bar 10 um.

Supplemental Movie 2: (See Figures 6; S5) Cell division followed by QBrain. Time-series (13h), collected at 6 minute intervals and displayed at 3 fps. Red: Histone::RFP; Green: Jupiter::GFP; heatmap (right hand panel overlay): probability of NB division (average of 5 frames, background subtracted for ease of viewing). Red indicates high probability of a NB division. Scale bar 10 um.